Research in Astronomy and Astrophysics, 24:055005 (26pp), 2024 May https://doi.org/10.1088/1674-4527/ad392c

Close Major-merger Pairs at $z = 0$: Star-forming Galaxies with Pseudobulges

Chuan He (何川)[1,2], Cong Xu (徐聪)[1], Ute Lisenfeld[3,4], Yu Sophia Dai (戴昱)[1], Taotao Fang (方陶陶)[5], Jiasheng Huang (黄家声)[1], Wei Wang (王炜)[1,6], and Qingzheng Yu (余清正)[5]
[1] Chinese Academy of Sciences South America Center for Astronomy, National Astronomical Observatories, Chinese Academy of Sciences, Beijing 100101, China; hechuan@nao.cas.cn, congxu@nao.cas.cn
[2] School of Astronomy and Space Sciences, University of Chinese Academy of Sciences, Beijing 100049, China
[3] Departamento de Física Teórica y del Cosmos, Universidad de Granada, 18071 Granada, Spain
[4] Instituto Carlos I de Física Téorica y Computacional, Facultad de Ciencias, 18071 Granada, Spain
[5] Department of Astronomy, Xiamen University, Xiamen 361005, China
[6] CAS Key Laboratory of Optical Astronomy, National Astronomical Observatories, Chinese Academy of Sciences, Beijing 100101, China
Received 2024 February 8; revised 2024 March 20; accepted 2024 March 28; published 2024 May 2

Abstract

We present a study of star-forming galaxies (SFGs) with pseudobulges (bulges with Sérsic index $n < 2$) in a local close major-merger galaxy pair sample (H-KPAIR). With data from new aperture photometries in the optical and near-infrared bands (aperture size of 7 kpc) and from the literature, we find that the mean Age of central stellar populations in Spirals with pseudobulges is consistent with that of disky galaxies and is nearly constant against the bulge-to-total ratio (B/T). Paired Spirals have a slightly lower fraction of pure disk galaxies ($B/T \leqslant 0.1$) than their counterparts in the control sample. Compared to SFGs with classical bulges, those with pseudobulges have a higher ($>2\sigma$) mean of specific star formation rate (sSFR) enhancement ($sSFR_{enh} = 0.33 \pm 0.07$ versus $sSFR_{enh} = 0.12 \pm 0.06$) and broader scatter (by $\sim$1 dex). The eight SFGs that have the highest $sSFR_{enh}$ in the sample all have pseudobulges. A majority (69%) of paired SFGs with strong enhancement (having sSFR more than 5 times the median of the control galaxies) have pseudobulges. The Spitzer data show that the pseudobulges in these galaxies are tightly linked to nuclear/circum-nuclear starbursts. Pseudobulge SFGs in S+S and in S+E pairs have significantly ($>3\sigma$) different sSFR enhancement, with the means of $sSFR_{enh} = 0.45 \pm 0.08$ and -0.04 ± 0.11, respectively. We find a decrease in the sSFR enhancements with the density of the environment for SFGs with pseudobulges. Since a high fraction (5/11) of pseudobulge SFGs in S+E pairs are in rich groups/clusters (local density $N_{1Mpc} \geqslant 7$), the dense environment might be the cause for their low $sSFR_{enh}$.

Key words: galaxies: evolution – galaxies: interactions – galaxies: star formation – galaxies: structure – galaxies: bulges – galaxies: photometry

1. Introduction

Broad and intensive studies have shown that galaxy interaction can induce star formation enhancement (Toomre & Toomre 1972; Larson & Tinsley 1978; Kennicutt et al. 1987; Xu & Sulentic 1991; Sanders & Mirabel 1996). Both simulations and observations have indicated that the existence and intensity of such enhancement are affected by many factors of the pair such as separation distance (Alonso et al. 2004; Nikolic et al. 2004), mass ratio (Cox et al. 2008), environment (Ellison et al. 2010), interaction phase (Scudder et al. 2012), orbital parameters (Patton et al. 2013). Meanwhile, some factors of the paired galaxies such as stellar mass (Rodighiero et al. 2011), redshift (Madau & Dickinson 2014) and morphology (Kennicutt 1998) also do affect the star formation behavior themselves. On the other hand, many quenching mechanisms are reported such as mass (Peng et al. 2010), environment (Peng et al. 2012), AGN feedback (Kormendy & Ho 2013), and bulge-to-total ratios (B/T, Martig et al. 2009; Bluck et al. 2014). The combining effect of many factors especially when studying a big sample with a large range of parameters may bury potential results or even cause statistical bias. This inspires us to delve into the fundamental mechanism of the interaction-induced star formation. For instance, by investigating the kinematic asymmetry utilizing the recent IFS (integral field spectrograph) technique, Feng et al. (2020) reveal that the strength of the ongoing tidal effect during certain merging phases is a more basic indicator to understanding the intermittent star formation enhancement in galaxy pairs than projected separations. Also, the star formation rate (SFR) level is influenced by both the quantity of gas and its efficiency in forming stars. Lisenfeld et al. (2019) reveals that mergers in an earlier stage (i.e., pair) can take a lead in transferring atom gas to molecular gas, which makes the paired sample has a higher star formation efficiency (SFE) when calculating the total gas, however, no significant SFE enhancement is found in their pair sample when calculating the molecular gas. On the other hand, the later stage mergers, who always show their strong strength

Table 1
Spiral Galaxies in H-KPAIR

Name	z	pair_type	bulge_type	is_SFG	r_{mag} (mag)	B/T	$\log M_{star}$ ($M_{\odot}$)	$sSFR_{enh}$ (dex)	N_{1Mpc}
(1)	(2)	(3)	(4)	(5)	(6)	(7)	(8)	(9)	(10)
J00202580+0049350	0.0149	SE	p	1	13.66	0.11	10.44	0.34	2
J01183417−0013416	0.0453	SS	p	1	15.60	0.37	10.97	1.34	6
J01183556−0013594	0.0455	SS	c	1	14.96	0.01	10.57	0.57	6
J02110638−0039191	0.0177	SS	c	1	14.50	0.27	10.42	0.45	4
J02110832−0039171	0.0181	SS	c	0	13.62	0.73	10.63	−1.19	4
J03381222+0110088	0.0392	SE	c	1	15.19	0.12	10.67	0.75	10
J07543194+1648214	0.0459	SS	p	1	14.63	0.03	10.95	0.71	3
J07543221+1648349	0.0462	SS	p	1	14.53	0.15	11.15	0.62	3
J08083377+3854534	0.0402	SE	c	1	15.45	0.86	10.73	0.11	16
J08233266+2120171	0.0181	SS	p	1	14.42	0.26	10.08	0.39	8
J08233421+2120515	0.0181	SS	c	1	13.80	0.39	10.35	0.55	8
J08291491+5531227	0.0251	SS	p	1	14.09	0.03	10.56	0.32	3
J08292083+5531081	0.0252	SS	p	1	14.04	0.11	10.71	0.18	3
J08364482+4722188	0.0526	SS	p	1	15.18	0.19	11.02	−0.46	9
J08364588+4722100	0.0526	SS	c	0	14.96	0.87	11.17	−0.67	9
J08381759+3054534	0.0476	SS	c	1	15.79	0.75	10.77	0.24	3
J08381795+3055011	0.0481	SS	c	1	15.09	0.73	11.08	−0.37	3
J08390125+3613042	0.0548	SE	c	1	15.51	0.71	10.94	−0.06	6
J08414959+2642578	0.0848	SE	p	1	15.43	0.46	11.44	−0.54	12
J09060498+5144071	0.0291	SE	c	1	14.34	0.14	10.60	0.08	4
J09123676+3547462	0.0235	SE	c	0	15.04	0.37	10.28	−1.15	6
J09134606+4742001	0.0527	SE	c	1	14.89	0.43	11.05	0.11	23
J09155467+4419510	0.0396	SS	p	1	14.97	0.00	10.76	1.11	2
J09155552+4419580	0.0396	SS	p	1	14.14	0.20	11.11	1.36	2
J09264111+0447247	0.0891	SS	c	1	16.21	1.00	11.12	−0.52	5
J09264137+0447260	0.0907	SS	c	0	16.17	0.70	11.40	−0.82	5
J09374413+0245394	0.0242	SE	c	1	12.85	0.09	11.24	0.60	3
J10100079+5440198	0.0460	SS	c	1	14.90	0.00	10.89	0.79	23
J10100212+5440279	0.0463	SS	c	1	15.67	0.29	10.85	0.29	23
J10155257+0657330	0.0299	SE	p	1	15.09	0.33	10.51	−0.82	3
J10205188+4831096	0.0530	SE	c	1	16.11	0.34	10.60	0.05	2
J10225647+3446564	0.0554	SS	p	1	15.99	0.35	10.67	0.41	2
J10225655+3446468	0.0564	SS	c	0	15.03	0.93	11.02	−0.87	2
J10233658+4220477	0.0456	SS	p	1	15.00	0.14	10.79	0.49	6
J10233684+4221037	0.0454	SS	p	1	15.84	0.63	10.55	0.43	6
J10272950+0114490	0.0236	SE	p	1	14.34	0.52	10.48	0.32	5
J10325316+5306536	0.0640	SE	c	1	15.49	0.72	11.05	−0.41	19
J10332972+4404342	0.0523	SS	p	1	14.79	0.26	11.12	0.84	4
J10333162+4404212	0.0521	SS	p	1	15.65	0.13	10.95	0.24	4
J10364274+5447356	0.0458	SE	c	0	15.34	0.79	10.81	−1.12	7
J10392338+3904501	0.0435	SE	p	0	15.26	0.38	10.77	−1.11	2
J10435053+0645466	0.0287	SS	c	1	14.26	0.11	10.55	0.70	5
J10435268+0645256	0.0281	SS	p	1	14.66	0.23	10.48	−0.25	5
J10452478+3910298	0.0268	SE	c	1	14.44	0.46	10.68	−0.34	4
J10514450+5101303	0.0238	SE	c	0	14.06	0.56	10.85	−0.76	8
J10595915+0857357	0.0627	SE	c	0	15.63	0.48	10.90	−0.71	9
J11014364+5720336	0.0478	SE	c	1	15.85	0.55	10.58	0.14	6
J11064944+4751119	0.0643	SS	c	0	15.48	0.87	11.02	−0.83	4
J11065068+4751090	0.0654	SS	p	1	15.23	0.13	11.09	0.40	4
J11204657+0028142	0.0255	SS	c	1	14.37	0.96	10.54	−0.12	7
J11204801+0028068	0.0256	SS	c	0	13.86	0.47	10.91	−0.91	7
J11251704+0227007	0.0504	SS	c	0	15.73	0.52	10.79	−0.73	5
J11251716+0226488	0.0507	SS	c	1	15.01	0.59	11.04	−0.16	5
J11273289+3604168	0.0351	SS	c	1	14.36	0.54	10.90	−0.13	5
J11273467+3603470	0.0351	SS	c	1	13.86	0.11	11.23	0.39	5
J11375801+4728143	0.0339	SE	c	0	14.64	0.59	10.81	−0.70	5

Table 1
(Continued)

Name	z	pair_type	bulge_type	is_SFG	r_{mag} (mag)	B/T	$\log M_{star}$ ($M_{\odot}$)	$sSFR_{enh}$ (dex)	N_{1Mpc}
(1)	(2)	(3)	(4)	(5)	(6)	(7)	(8)	(9)	(10)
J11440433+3332339	0.0315	SE	p	1	15.38	0.15	10.40	0.24	16
J11484370+3547002	0.0641	SS	p	1	16.50	0.23	10.97	0.38	5
J11484525+3547092	0.0636	SS	c	1	14.77	0.13	11.27	0.53	5
J11501333+3746107	0.0550	SS	c	1	15.56	0.54	10.88	−0.32	2
J11501399+3746306	0.0555	SS	c	1	15.19	0.10	10.95	0.09	2
J11505764+1444200	0.0572	SE	c	0	15.94	0.59	10.92	−0.96	5
J11542299+4932509	0.0702	SE	c	0	15.92	0.21	10.98	−0.80	3
J12020424+5342317	0.0647	SE	c	1	16.01	0.89	10.93	0.06	3
J12054066+0135365	0.0220	SE	p	0	14.52	0.26	10.33	−1.09	16
J12115507+4039182	0.0229	SS	c	1	14.51	0.40	10.44	0.08	5
J12115648+4039184	0.0235	SS	c	1	14.87	0.13	10.42	0.60	5
J12191866+1201054	0.0268	SE	p	1	15.14	0.37	10.20	−0.01	7
J12433887+4405399	0.0418	SE	c	1	14.84	0.15	10.89	−0.13	3
J12525011+4645272	0.0613	SE	p	1	15.47	0.10	11.08	−0.30	4
J13011662+4803366	0.0303	SS	p	1	14.55	0.50	10.49	0.64	6
J13011835+4803304	0.0298	SS	p	1	15.16	0.22	10.31	0.65	6
J13082737+0422125	0.0255	SS	c	1	15.61	0.03	9.88	−0.30	1
J13082964+0422045	0.0257	SS	c	1	14.80	0.40	10.29	−0.38	1
J13131470+3910382	0.0716	SE	c	1	16.36	0.43	10.95	−0.48	15
J13151386+4424264	0.0359	SS	c	1	14.55	0.20	10.74	0.00	3
J13151726+4424255	0.0357	SS	c	1	14.26	0.94	11.08	0.70	3
J13153076+6207447	0.0306	SS	p	1	14.59	0.26	10.59	0.64	2
J13153506+6207287	0.0306	SS	p	1	14.57	0.16	10.77	1.59	2
J13325525−0301347	0.0493	SS	p	1	15.61	0.51	10.67	0.62	3
J13325655−0301395	0.0483	SS	c	1	14.81	0.05	10.93	0.26	3
J13462001−0325407	0.0248	SE	c	0	13.97	0.68	10.79	−0.62	3
J14003661−0254327	0.0256	SS	c	0	14.26	0.70	10.72	−1.33	12
J14003796−0254227	0.0269	SS	c	0	14.76	0.49	10.66	−0.82	13
J14005783+4251203	0.0327	SS	p	1	15.10	0.02	10.76	0.82	2
J14005879+4250427	0.0335	SS	p	1	15.25	0.38	10.65	0.95	2
J14055079+6542598	0.0306	SE	p	1	15.49	0.29	10.34	−0.06	7
J14062157+5043303	0.0065	SE	p	1	12.00	0.05	10.18	0.17	3
J14070703−0234513	0.0586	SE	c	1	15.55	0.13	11.05	−0.19	4
J14234238+3400324	0.0136	SS	p	1	13.55	0.28	10.11	0.29	4
J14234632+3401012	0.0126	SS	p	1	13.91	0.17	10.26	−0.36	4
J14245831−0303597	0.0525	SS	c	1	15.02	0.05	10.92	0.04	3
J14245913−0304012	0.0535	SS	c	0	15.00	0.18	11.18	−0.67	3
J14250739+0313560	0.0375	SE	c	0	15.64	0.55	10.44	−1.10	5
J14294766+3534275	0.0290	SS	c	1	13.75	0.56	11.04	−0.17	8
J14295031+3534122	0.0296	SS	p	1	14.62	0.14	10.67	−0.07	9
J14334683+4004512	0.0260	SS	c	1	13.48	0.44	10.99	0.53	4
J14334840+4005392	0.0264	SS	c	1	13.91	0.80	10.83	0.30	4
J14442055+1207429	0.0304	SS	c	1	14.44	0.42	10.83	0.15	3
J14442079+1207552	0.0314	SS	c	1	13.59	0.28	11.17	0.16	3
J15002500+4317131	0.0316	SE	c	0	14.57	0.40	10.80	−1.31	4
J15053137+3427534	0.0745	SE	c	0	15.80	0.84	11.03	−0.71	9
J15064391+0346364	0.0363	SS	c	0	14.28	0.54	11.01	−0.66	8
J15064579+0346214	0.0352	SS	c	1	14.68	0.46	10.93	0.54	8
J15101587+5810425	0.0303	SS	c	0	14.63	0.35	10.73	−0.97	1
J15101776+5810375	0.0317	SS	p	1	15.65	0.29	10.53	0.05	1
J15144544+0403587	0.0386	SS	c	0	15.04	0.52	10.91	−0.50	14
J15144697+0403576	0.0392	SS	c	0	14.82	0.48	10.85	−0.95	14
J15233768+3749030	0.0234	SE	p	1	15.04	0.16	10.18	−0.08	3
J15264774+5915464	0.0447	SE	c	0	15.07	0.81	10.82	−1.00	7
J15281276+4255474	0.0188	SS	p	1	13.12	0.31	11.04	−0.16	8
J15281667+4256384	0.0180	SS	c	0	13.40	0.77	10.77	−0.98	8

Table 1
(Continued)

Name	z	pair_type	bulge_type	is_SFG	r_{mag} (mag)	B/T	$\log M_{star}$ ($M_\odot$)	$sSFR_{enh}$ (dex)	N_{1Mpc}
(1)	(2)	(3)	(4)	(5)	(6)	(7)	(8)	(9)	(10)
J15523393+4620237	0.0610	SE	c	1	15.60	0.27	10.94	0.22	7
J15562191+4757172	0.0191	SE	p	1	14.71	0.04	10.19	0.23	9
J15583749+3227379	0.0494	SS	p	0	16.15	0.47	10.60	−1.14	3
J15583784+3227471	0.0485	SS	p	1	15.18	0.60	10.91	0.32	3
J16024254+4111499	0.0335	SS	c	1	14.14	0.08	10.78	0.77	5
J16024475+4111589	0.0333	SS	p	1	15.18	0.02	10.46	0.43	5
J16080559+2529091	0.0415	SS	p	1	15.02	0.15	10.97	0.08	8
J16080648+2529066	0.0423	SS	p	1	14.71	0.39	11.23	−0.13	8
J16082261+2328459	0.0409	SS	c	1	15.00	0.04	10.39	0.20	4
J16082354+2328240	0.0408	SS	c	1	15.50	0.25	10.72	0.57	4
J16145418+3711064	0.0582	SE	c	0	14.64	0.74	11.17	−0.85	8
J16282497+4110064	0.0330	SS	c	0	14.01	0.41	10.93	−0.47	21
J16282756+4109395	0.0318	SS	c	0	14.19	0.55	10.89	−0.44	31
J16354293+2630494	0.0701	SE	c	0	15.22	0.66	11.27	−0.59	28
J16372583+4650161	0.0578	SS	c	1	14.99	0.49	11.30	−0.37	5
J16372754+4650054	0.0568	SS	p	1	15.14	0.02	10.98	−0.09	5
J17020378+1859495	0.0558	SE	c	1	16.55	0.36	10.72	−0.78	6
J17045089+3448530	0.0572	SS	c	1	15.99	0.48	10.75	0.80	4
J17045097+3449020	0.0563	SS	p	1	15.26	0.28	10.98	1.04	4
J20471908+0019150	0.0130	SE	c	1	11.85	0.34	11.09	−0.13	7

Note. The columns are: (1) galaxy name; (2) redshift; (3) pair type: "S" for Spiral+Spiral pair, "S" for Spiral+Elliptical pair; (4) if the galaxy is an SFG, 1 for true and 0 for false; (5) bulge type: "p" for pseudobulge, "c" for classical-bulge; (6) magnitude of r-band; (7) Bulge-to-Total ratio; (8) stellar mass; (9) specific star formation rate enhancement; (10) number of galaxies brighter than $M_r = -19.7$ mag within a D = 1 Mpc circle centered on the galaxy.

on star formation activities by appearing as a ULIRG, can pool a large amount of molecular gas (e.g., Sargent & Scoville 1991; Scoville et al. 1991). By controlling the total gas content, Li et al. (2023) found no significant enhancement on SFE in paired galaxies compared to the single galaxies. To conclude, it is still controversial whether and how galaxy interaction can induce star formation enhancement. To acquire solid evidence, one needs to select the sample and their controls carefully, and a detailed classification of their sample as well.

Far-infrared (FIR) observations by Spitzer (Xu et al. 2010) and Herschel (Cao et al. 2016) on a complete, unbiased close major-merger pairs sample selected from K_s-band Domingue et al. (2009) suggest that only star-forming galaxies (SFGs) in spiral-spiral (hereafter S+S) pairs have significantly enhanced specific star formation rate (sSFR = SFR/Mstar), but not those in Spiral-Elliptical (hereafter S+E) pairs. This situation is also presented in Park & Choi (2009), Hwang et al. (2010), Xu et al. (2010), Moon et al. (2019). He et al. (2022) studied the dependence of the interaction-induced specific star formation rate enhancement ($sSFR_{enh} = \log(sSFR_{pg}) - \log(sSFR_{med,ctrl})$ where "pg" stands for paired galaxy and "med,ctrl" for the median of their control galaxies) on the bulge-to-total ratio (B/T). They found a negative dependence of the interaction-induced sSFR enhancement on the bulge-to-total ratio (B/T) and a significant ($>5\sigma$) enhancement only in paired SFGs with $B/T < 0.3$. This is consistent with the results of theoretical simulations which predicted that a massive bulge can stabilize the disk and suppress the SFR during and after close encounters (Mihos & Hernquist 1996; Cox et al. 2008; Di Matteo et al. 2008). However, it appears that SFGs with low B/T ratios, in particular the disky galaxies ($B/T \leqslant 0.1$), have very diversified $sSFR_{enh}$ with the value varying in a range of ∼2.5 orders of magnitude, and even some of such SFGs have sSFR deficit.

In their analysis, He et al. (2022) separated pseudobulges (with Sérsic index $n < 2$) from classical bulges (with Sérsic index $n \geqslant 2$) and assigned $B/T = 0$ to galaxies with pseudobulges. This is because many pseudobulges found in two-component (bulge and disk) models (such as those in He et al. 2022) are misidentified bars, nuclear disks, and nuclear rings (Kormendy & Kennicutt 2004) which themselves may be triggered by interaction (Chown et al. 2019; Erwin et al. 2021). Meanwhile, the pseudobulges unrelated to nuclear star formation are mostly found in late-type spirals with relatively low B/T ratios (Kim et al. 2016), and assigning them to disky galaxies shall not introduce strong bias. However, bars and nuclear rings often have intermittent star formation activity and, when being caught in the "off" phase, may appear to be SFR-quenched (Fraser-McKelvie et al. 2020). Also, some massive early-type spirals (such as S0 and Sa galaxies) with

low gas content and low SFR may have large bars (Herrera-Endoqui et al. 2017).

Can the broader scatter of the $sSFR_{enh}$ among disky SFGs be due to the diversity of galaxies with pseudobulges? The major scientific goal of this paper is to answer the above question and to investigate the roles played by pseudobulge SFGs regarding sSFR enhancement in paired galaxies. Different from He et al. (2022), for galaxies with pseudobulges, we use the original B/T values instead of assigning $B/T = 0$. The SFG sample we use in this paper is introduced in Section 2. In Section 3 we present a study of the optical color–color diagrams measured in the inner part of the paired galaxies, particularly for galaxies with pseudobulges to separate those with bars, nuclear disks, and nuclear rings from normal pseudobulges of $n < 2$. In Section 4 we present our science analyses and results. A discussion is carried out in Section 5. We conclude our paper in Section 6. Throughout this paper, we adopt the Λ-cosmology with $\Omega_m = 0.3$ and $\Omega_\Lambda = 0.7$, and $H_0 = 70\,km\,s^{-1}\,Mpc^{-1}$.

2. The Sample

The sample we use in this paper is the same as that in He et al. (2022), which is the local close major-merger sample H-KPAIR (Cao et al. 2016). H-KPAIR is a subsample of the KPAIR which is a complete and unbiased K_s-band (Two Micron All Sky Survey, 2MASS) selected pair sample (Domingue et al. 2009). The H-KPAIR includes 44 Spiral+Spiral (S+S) pairs and 44 Spiral+Elliptical (S+E) pairs, all of which have spectroscopic redshifts in the range of $0.0067 < z < 0.1$, the projected separations in the range of $5\,h^{-1}\,kpc \leqslant s(p) \leqslant 20\,h^{-1}\,kpc$, the radial relative velocity $\delta(Vz) < 500\,km\,s^{-1}$ and the K_s-band magnitude differences within 1 mag (corresponding to a mass ratio no greater than 2.5). The strict selection criteria of H-KPAIR gather the most enhanced closed major-merger pairs and makes it an ideal sample to explore the interaction effect to the paired galaxies. All galaxies in H-KPAIR have Herschel imaging observations in the six bands at 70, 110, 160, 250, 350 and 500, and their SFRs are derived from the Herschel data (Cao et al. 2016). 70 pairs have GBT 21 cm HI observations (Zuo et al. 2018), and 78 spiral galaxies are observed by the IRAM 30 m telescope for the CO emissions (Lisenfeld et al. 2019). The B/T ratios of H-KPAIR galaxies are taken from He et al. (2022) which are based on 2D decompositions carried out using the SDSS r-band image. The stellar masses are also taken from He et al. (2022) who updated the formalism of Cao et al. (2016) by including a $(g - r)$ color correction when estimating the mass from the K_s-band luminosity. Throughout this paper, we mainly focus on two subsamples of H-KPAIR: (1) all spiral galaxies Sections 3 and 4.1 and (2) all star-forming galaxies (SFGs; Sections 4.2 and 4.3). Following Cao et al. (2016) and He et al. (2022), SFGs are defined by having $\log(sSFR/yr^{-1}) \geqslant -11.3$. There are 98 SFGs out of 132 Spirals (Table 1) in the H-KPAIR sample.

3. Galaxy Central Colors

We carry out aperture photometry for all galaxies in the H-KPAIR sample using a consistent round aperture in images of the SDSS u, r, i and 2MASS K_s-bands. The u, r, i images are generated using SDSS SAS mosaic tool,[7] which can stitch together several sky-subtracted, calibrated frames[8] to form a coherent image over a specified patch of sky using the SWarp (Bertin et al. 2002). For the K_s-band, the 2MASS images are resampled into the same pixel scale as the SDSS images of $0\farcs396\,pix^{-1}$, and the background are subtracted with SWarp. The median Full-Width-at-Half-Maximum (FWHM) of the point-spread function (PSF) in the four bands are $1\farcs53$, $1\farcs32$, $1\farcs26$ and $2\farcs9$, respectively.

For each galaxy, we use the same aperture in all four bands which corresponds to a projected diameter of 7 kpc and is centered at its SDSS coordinates. Such a setup is to avoid overlap between apertures of the two member galaxies in a pair, given the minimal pair separation of $5\,h^{-1}\,kpc$ (corresponding approximately to 7 kpc for $H_0 = 70\,km\,s^{-1}\,Mpc^{-1}$). Also, the aperture diameters corresponding to 7 kpc on our sources range from $4\farcs2$ to $53''$, and most galaxies (141/176) have diameters larger than 2 times $2\farcs9$, which is the worst resolution of the data (i.e., the FWHM = $2\farcs9$ for the K_s-band). Therefore no aperture correction is needed for any photometry.

The photometric errors of SDSS bands are calculated by combining the Poissonian error of the source flux, the rms of background, and the calibration error.[9,10] Given the good S/N of our galaxies in the optical bands, errors in these bands are dominated by the calibration error (1% for the r and i-bands and 2% for the u-band). For the 2MASS K_s-band, in addition to the error sources described above, the coadd noise caused by the resampling and smoothing when generating the Atlas Images is also considered.[11]

The spiral galaxies in the sample have a median bulge size of $2 \times R_e = 3.6$ kpc (R_e: effective radius of the bulge), and 26% of them have $2 \times R_e \geqslant 7$ kpc. For the latter galaxies, the colors derived from the 7 kpc aperture photometries provide information on the stellar population within the bulge. For the rest galaxies in the sample, the 7 kpc aperture can include stellar radiations both in the bulge and a small portion of the inner disk, and their relative importance depends on the B/T ratio. As shown in Figure 1, there is a significant correlation between bulge size and B/T (the Spearman's rank correlation coefficient $r_S = 0.55$ and the significance $p_S = 5.6\,e^{-12}$).

[7] https://dr12.sdss.org/mosaics/
[8] https://data.sdss.org/datamodel/files/BOSS_PHOTOOBJ/frames/RERUN/RUN/CAMCOL/frame.html
[9] https://data.sdss.org/datamodel/files/BOSS_PHOTOOBJ/frames/RERUN/RUN/CAMCOL/frame.html
[10] https://www.sdss4.org/dr12/algorithms/fluxcal/
[11] https://irsa.ipac.caltech.edu/data/2MASS/docs/releases/allsky/doc/sec6_8a.html

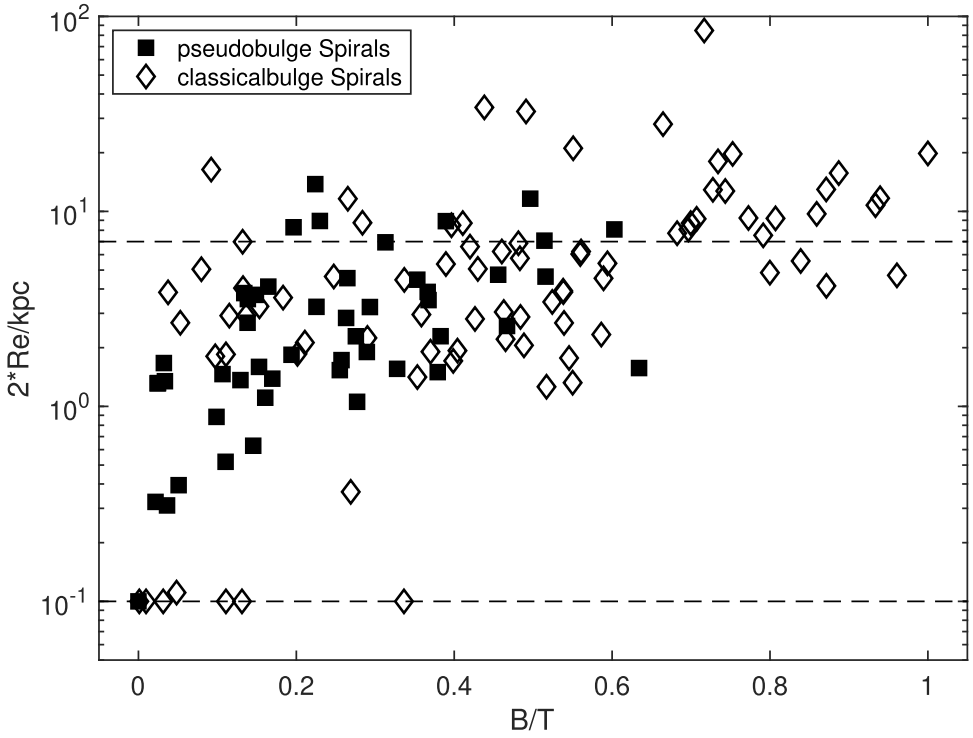

Figure 1. Plot of bulge size ($2 \times R_e$) vs. B/T ratio of all spiral galaxies in H-KPAIR. The horizontal dashed line corresponds to the aperture size of our photometry (D = 7 kpc) and a lower cut at $2 \times R_e = 0.1$ kpc (sources with bulge sizes below this line are plotted on it). The filled squares represent galaxies with pseudobulges and the open diamonds denote galaxies with classical bulges.

To interpret the colors, predictions of broad-band fluxes are calculated using the Simple Stellar Population (SSP, or instantaneous-burst) model of Bruzual & Charlot (2003), with the time after the instantaneous-burst τ (i.e., stellar age) and the attenuation A_v as the free parameters. The model uses the Padova (1994) evolution tracks, the Chabrier (2003) IMF with lower and upper mass cutoffs of 0.1–100 $M_\odot$, and the solar metallicity ($Z = 0.02$). The extinctions are calculated following the formalism of Cardelli et al. (1989) for the standard diffuse interstellar medium. It is worth noting that the SSP model may be an over-simplification of the real stellar populations in question, and the model predictions on the τ and A_v have large uncertainties. Nevertheless, the model provides a framework to link the colors to the physical properties (e.g., the Age) of the stellar populations which allows us to investigate the difference between galaxies with pseudobulges and classical bulges using color–color diagrams. The results of our aperture photometry and the model fits are listed in Table 2.

4. Results

4.1. Difference Between Pseudobulges and Classical Bulges

Two *u-r* versus *i-K*$_s$ color–color diagrams are presented in Figures 2 and 3, with the false color scale representing the B/T ratio and sSFR$_{enh}$, respectively. The region outlined by the red contour (with a red label "E") in the upper-left corner of the diagram is where the elliptical galaxies (not plotted) are found. Most Spirals located in this region are those with relatively large classical bulges and low sSFR$_{enh}$. The mesh grid in the diagram consists of lines for fixed values of τ and attenuation A_v, respectively, as predicted by the SSP model (see Section 3). According to the model, galaxies in the region "E" have old stellar populations of Age $>$ 1 Gyr in their central part. For the remaining galaxies, most have their central stellar populations with Ages in the range of [0.1, 1] Gyr and very few with young Ages in the range of [0.01, 0.1] Gyr which are likely associated with nuclear/circum-nuclear starbursts. The range of A_v is between 0 and 3 mag, with most galaxies having 1 mag $< A_v <$ 2.5 mag.

We estimate the Age and A_v for each galaxy via interpolations among the model predictions (in the mesh grid) adjacent to its position in the color–color diagram. Galaxies with Age $>$ 13 Gyr are regarded as Age = 13 Gyr and galaxies with $A_v < 0$ are regarded as $A_v = 0$. The plot of A_v versus Age (Figure 4) shows a strong anti-correlation between the two variables, which is understandable because younger stellar populations are usually associated with stronger star formation activity and higher dust attenuation, and older stellar

Table 2
Aperture Photometry and Model fits of the H-KPAIR Sample

Name	Type	m_u (mag)	e_u (mag)	m_r (mag)	e_r (mag)	m_i (mag)	e_i (mag)	m_{K_s} (mag)	e_{K_s} (mag)	Age (Gyr)	A_v (mag)
(1)	(2)	(3)	(4)	(5)	(6)	(7)	(8)	(9)	(10)	(11)	(12)
J00202580+0049350	S	16.86	0.02	14.51	0.01	14.09	0.01	13.34	0.02	0.56	1.25
J00202748+0050009	E	16.48	0.02	13.87	0.01	13.44	0.01	12.71	0.01	3.21	0.61
J01183417−0013416	S	18.51	0.03	16.17	0.01	15.65	0.01	14.18	0.07	0.05	2.85
J01183556−0013594	S	18.17	0.03	16.55	0.01	16.24	0.01	15.66	0.05	0.09	1.54
J02110638−0039191	S	17.75	0.03	15.25	0.01	14.77	0.01	13.50	0.02	0.10	2.77
J02110832−0039171	S	16.30	0.02	13.91	0.01	13.54	0.01	12.92	0.01	1.61	0.67
J03381222+0110088	S	18.67	0.03	16.39	0.01	15.92	0.01	14.97	0.04	0.17	2.02
J03381299+0109414	E	18.94	0.03	16.09	0.01	15.63	0.01	14.76	0.08	6.31	0.61
J07543194+1648214	S	18.17	0.03	15.93	0.01	15.52	0.01	14.44	0.28	0.09	2.42
J07543221+1648349	S	17.75	0.02	15.64	0.01	15.23	0.01	14.35	0.26	0.13	2.01
J08083377+3854534	S	18.34	0.03	16.01	0.01	15.61	0.01	14.84	0.04	0.46	1.34
J08083563+3854522	E	18.27	0.03	15.49	0.01	15.05	0.01	14.24	0.02	6.07	0.53
J08233266+2120171	S	16.10	0.02	14.73	0.01	14.53	0.01	14.07	0.09	0.07	1.26
J08233421+2120515	S	16.07	0.02	14.47	0.01	14.21	0.01	13.67	0.06	0.09	1.48
J08291491+5531227	S	17.57	0.03	15.37	0.01	14.97	0.01	14.25	0.02	0.34	1.36
J08292083+5531081	S	17.24	0.02	14.84	0.01	14.44	0.01	13.70	0.01	0.72	1.16
J08364482+4722188	S	18.99	0.03	16.28	0.01	15.83	0.01	14.95	0.03	1.74	1.11
J08364588+4722100	S	18.66	0.03	15.84	0.01	15.41	0.01	14.57	0.02	7.35	0.48
J08381759+3054534	S	18.73	0.03	16.34	0.01	15.85	0.01	14.84	0.02	0.19	2.09
J08381795+3055011	S	19.00	0.03	16.07	0.01	15.52	0.01	14.31	0.01	0.61	2.05
J08385973+3613164	E	18.58	0.03	15.74	0.01	15.30	0.01	14.53	0.03	13.00	0.12
J08390125+3613042	S	19.00	0.03	16.35	0.01	15.89	0.01	15.01	0.05	0.98	1.32
J08414959+2642578	S	19.65	0.03	16.69	0.01	16.16	0.01	15.21	0.03	6.62	0.75
J08415054+2642475	E	20.02	0.04	17.09	0.01	16.63	0.01	16.08	0.05	13.00	0.00
J09060283+5144411	E	17.61	0.02	14.91	0.01	14.52	0.01	13.74	0.02	4.52	0.56
J09060498+5144071	S	17.99	0.03	15.59	0.01	15.20	0.01	14.49	0.03	0.86	1.05
J09123636+3547180	E	17.15	0.02	14.58	0.01	14.18	0.01	13.56	0.01	7.19	0.12
J09123676+3547462	S	17.65	0.02	15.25	0.01	14.87	0.01	14.34	0.02	4.52	0.13
J09134461+4742165	E	18.57	0.03	15.75	0.01	15.31	0.01	14.56	0.02	13.00	0.02
J09134606+4742001	S	17.54	0.02	15.98	0.01	15.49	0.01	14.43	0.01	0.04	1.86
J09155467+4419510	S	18.19	0.03	15.85	0.01	15.40	0.01	14.22	0.01	0.09	2.60
J09155552+4419580	S	17.58	0.02	15.45	0.01	15.03	0.01	13.93	0.01	0.07	2.39
J09264111+0447247	S	20.02	0.04	17.18	0.01	16.73	0.01	15.98	0.15	13.00	0.00
J09264137+0447260	S	20.03	0.04	17.11	0.01	16.65	0.01	15.69	0.11	4.26	0.93
J09374413+0245394	S	16.77	0.02	14.41	0.01	13.97	0.01	12.83	0.01	0.10	2.57
J09374506+0244504	E	16.79	0.02	14.00	0.01	13.57	0.01	12.72	0.01	4.36	0.72
J10100079+5440198	S	18.61	0.03	16.46	0.01	16.01	0.01	14.91	0.01	0.07	2.39
J10100212+5440279	S	18.46	0.03	16.26	0.01	15.83	0.01	14.96	0.01	0.18	1.86
J10155257+0657330	S	17.87	0.02	15.57	0.01	15.20	0.01	14.60	0.15	0.92	0.84
J10155338+0657495	E	17.41	0.02	14.79	0.01	14.38	0.01	13.66	0.07	3.77	0.54
J10205188+4831096	S	19.31	0.03	17.00	0.01	16.56	0.01	15.76	0.06	0.36	1.48
J10205369+4831246	E	19.07	0.03	16.18	0.01	15.72	0.01	14.86	0.03	9.75	0.43
J10225647+3446564	S	18.90	0.03	16.70	0.01	16.27	0.01	15.41	0.05	0.18	1.84
J10225655+3446468	S	18.33	0.03	15.79	0.01	15.41	0.01	14.76	0.03	4.26	0.37
J10233658+4220477	S	17.76	0.02	16.02	0.01	15.62	0.01	14.82	0.01	0.06	1.83
J10233684+4221037	S	17.89	0.02	16.28	0.01	15.88	0.01	15.15	0.02	0.06	1.68
J10272950+0114490	S	17.24	0.02	15.15	0.01	14.79	0.01	13.83	0.05	0.09	2.21
J10272970+0115170	E	16.93	0.02	14.31	0.01	13.90	0.01	13.23	0.03	6.78	0.22
J10325316+5306536	S	19.31	0.03	16.58	0.01	16.11	0.01	15.27	0.05	3.12	0.81
J10325321+5306477	E	18.82	0.03	16.01	0.01	15.57	0.01	14.83	0.03	13.00	0.00
J10332972+4404342	S	17.72	0.02	15.64	0.01	15.22	0.01	14.35	0.01	0.11	2.04
J10333162+4404212	S	19.40	0.04	16.76	0.01	16.26	0.01	15.01	0.02	0.17	2.56
J10364274+5447356	S	18.95	0.03	16.27	0.01	15.87	0.01	15.09	0.12	3.48	0.68
J10364400+5447489	E	17.93	0.02	15.28	0.01	14.88	0.01	14.15	0.05	4.85	0.45
J10392338+3904501	S	18.69	0.03	15.94	0.01	15.54	0.01	14.78	0.02	8.30	0.30
J10392515+3904573	E	18.36	0.03	15.64	0.01	15.24	0.01	14.53	0.01	10.62	0.14
J10435053+0645466	S	16.29	0.02	15.05	0.01	14.83	0.01	14.15	0.02	0.04	1.31

Table 2
(Continued)

Name	Type	m_u	e_u	m_r	e_r	m_i	e_i	m_{K_s}	e_{K_s}	Age	A_v
		(mag)	(mag)	(mag)	(mag)	(mag)	(mag)	(mag)	(mag)	(Gyr)	(mag)
(1)	(2)	(3)	(4)	(5)	(6)	(7)	(8)	(9)	(10)	(11)	(12)
J10435268+0645256	S	18.08	0.03	15.64	0.01	15.24	0.01	14.37	0.02	0.43	1.54
J10452478+3910298	S	17.51	0.02	15.00	0.01	14.60	0.01	13.89	0.02	1.70	0.81
J10452496+3909499	E	17.43	0.02	14.81	0.01	14.41	0.01	13.73	0.26	5.86	0.30
J10514368+5101195	E	16.65	0.02	13.96	0.01	13.55	0.01	12.78	0.01	4.72	0.53
J10514450+5101303	S	17.14	0.02	14.55	0.01	14.15	0.01	13.51	0.02	7.81	0.11
J10595869+0857215	E	18.92	0.03	16.06	0.01	15.64	0.01	14.95	0.02	13.00	0.00
J10595915+0857357	S	19.29	0.03	16.47	0.01	16.04	0.01	15.50	0.03	13.00	0.00
J11014357+5720058	E	18.21	0.03	15.65	0.01	15.30	0.01	14.66	0.02	5.65	0.25
J11014364+5720336	S	19.02	0.03	16.35	0.01	15.97	0.01	15.25	0.03	5.89	0.38
J11064944+4751119	S	18.50	0.03	15.89	0.01	15.55	0.01	14.85	0.01	4.69	0.41
J11065068+4751090	S	18.88	0.03	16.54	0.01	16.10	0.01	15.20	0.02	0.24	1.80
J11204657+0028142	S	16.73	0.02	14.60	0.01	14.31	0.01	13.71	0.02	0.48	1.03
J11204801+0028068	S	17.23	0.02	14.47	0.01	14.04	0.01	13.25	0.01	6.15	0.49
J11251704+0227007	S	18.82	0.03	16.14	0.01	15.73	0.01	14.99	0.03	5.13	0.46
J11251716+0226488	S	18.63	0.03	15.85	0.01	15.41	0.01	14.63	0.02	7.92	0.37
J11273289+3604168	S	17.68	0.02	15.12	0.01	14.74	0.01	13.97	0.02	1.36	1.01
J11273467+3603470	S	17.50	0.02	15.01	0.01	14.57	0.01	13.59	0.01	0.32	1.82
J11375476+4727588	E	17.35	0.02	14.69	0.01	14.29	0.01	13.53	0.01	4.00	0.58
J11375801+4728143	S	17.79	0.02	15.09	0.01	14.68	0.01	13.93	0.01	5.65	0.44
J11440335+3332062	E	17.89	0.03	15.18	0.01	14.76	0.01	13.84	0.02	1.02	1.38
J11440433+3332339	S	17.83	0.03	15.77	0.01	15.40	0.01	14.65	0.04	0.19	1.62
J11484370+3547002	S	20.53	0.06	17.90	0.01	17.25	0.01	15.59	0.04	0.05	3.26
J11484525+3547092	S	18.93	0.03	16.48	0.01	16.03	0.01	15.20	0.03	0.57	1.38
J11501333+3746107	S	18.89	0.03	16.22	0.01	15.80	0.01	15.09	0.03	6.71	0.31
J11501399+3746306	S	18.06	0.02	15.99	0.01	15.58	0.01	14.87	0.02	0.23	1.47
J11505764+1444200	S	19.49	0.03	16.68	0.01	16.24	0.01	15.43	0.03	7.53	0.45
J11505844+1444124	E	18.05	0.02	15.41	0.01	15.03	0.01	14.33	0.01	6.17	0.31
J11542299+4932509	S	19.98	0.04	17.30	0.01	16.88	0.01	16.19	0.07	9.27	0.15
J11542307+4932456	E	19.31	0.03	16.35	0.01	15.90	0.01	15.15	0.03	13.00	0.00
J12020424+5342317	S	20.00	0.05	17.04	0.01	16.50	0.01	15.58	0.02	9.36	0.55
J12020537+5342487	E	19.06	0.03	16.20	0.01	15.77	0.01	15.02	0.01	13.00	0.00
J12054066+0135365	S	17.37	0.02	14.90	0.01	14.52	0.01	13.94	0.02	4.29	0.26
J12054073+0134302	E	17.15	0.02	14.49	0.01	14.09	0.01	13.40	0.02	8.31	0.18
J12115507+4039182	S	16.51	0.02	14.68	0.01	14.37	0.01	13.79	0.01	0.16	1.38
J12115648+4039184	S	17.50	0.02	15.10	0.01	14.74	0.01	14.00	0.02	0.72	1.15
J12191719+1200582	E	17.82	0.03	15.17	0.01	14.77	0.01	14.09	0.03	7.98	0.18
J12191866+1201054	S	17.63	0.02	15.69	0.01	15.33	0.01	14.66	0.04	0.17	1.52
J12433887+4405399	S	18.73	0.03	16.07	0.01	15.66	0.01	14.95	0.03	6.43	0.32
J12433936+4406046	E	18.00	0.02	15.31	0.01	14.92	0.01	14.19	0.02	6.70	0.33
J12525011+4645272	S	18.98	0.03	16.48	0.01	16.05	0.01	15.37	0.03	2.10	0.69
J12525212+4645294	E	18.92	0.03	16.11	0.01	15.63	0.01	14.83	0.02	8.83	0.36
J13011662+4803366	S	16.20	0.02	15.00	0.01	14.80	0.01	14.29	0.02	0.05	1.18
J13011835+4803304	S	17.04	0.02	15.56	0.01	15.31	0.01	14.78	0.03	0.07	1.40
J13082737+0422125	S	17.67	0.02	15.98	0.01	15.70	0.01	15.36	0.06	0.28	0.75
J13082964+0422045	S	17.36	0.02	15.32	0.01	14.98	0.01	14.41	0.03	0.37	1.07
J13131429+3910360	E	19.15	0.03	16.26	0.01	15.84	0.01	15.13	0.02	13.00	0.00
J13131470+3910382	S	19.54	0.03	16.78	0.01	16.40	0.01	15.75	0.03	13.00	0.00
J13151386+4424264	S	17.40	0.02	15.46	0.01	15.12	0.01	14.38	0.19	0.13	1.74
J13151726+4424255	S	17.41	0.02	15.02	0.01	14.59	0.01	13.43	0.08	0.11	2.57
J13153076+6207447	S	17.33	0.02	15.56	0.01	15.23	0.01	14.06	0.02	0.04	2.13
J13153506+6207287	S	16.62	0.02	15.13	0.01	14.81	0.01	13.49	0.01	0.02	2.00
J13325525−0301347	S	18.60	0.03	16.37	0.01	15.95	0.01	15.05	0.02	0.17	1.93
J13325655−0301395	S	18.27	0.03	16.19	0.01	15.79	0.01	15.12	0.02	0.27	1.34
J13462001−0325407	S	17.21	0.02	14.62	0.01	14.22	0.01	13.48	0.02	2.57	0.71
J13462215−0325057	E	17.50	0.02	14.82	0.01	14.38	0.01	13.60	0.01	3.34	0.70
J14003661−0254327	S	17.54	0.02	14.91	0.01	14.50	0.01	13.79	0.01	4.94	0.41
J14003796−0254227	S	17.70	0.02	15.13	0.01	14.73	0.01	13.98	0.02	1.85	0.86

Table 2
(Continued)

Name	Type	m_u (mag)	e_u (mag)	m_r (mag)	e_r (mag)	m_i (mag)	e_i (mag)	m_{K_s} (mag)	e_{K_s} (mag)	Age (Gyr)	A_v (mag)
(1)	(2)	(3)	(4)	(5)	(6)	(7)	(8)	(9)	(10)	(11)	(12)
J14005783+4251203	S	18.53	0.03	15.94	0.01	15.43	0.01	14.20	0.03	0.16	2.54
J14005879+4250427	S	17.95	0.02	15.78	0.01	15.32	0.01	14.16	0.03	0.06	2.47
J14055079+6542598	S	18.47	0.03	15.98	0.01	15.54	0.01	14.72	0.09	0.66	1.34
J14055334+6542277	E	17.58	0.02	15.07	0.01	14.70	0.01	14.14	0.06	7.91	0.00
J14062157+5043303	S	14.02	0.02	12.46	0.01	12.20	0.01	11.78	0.01	0.13	1.19
J14064127+5043239	E	15.08	0.02	12.58	0.01	12.16	0.01	11.59	0.01	7.61	0.00
J14070703−0234513	S	19.56	0.04	16.73	0.01	16.24	0.01	15.39	0.04	5.96	0.61
J14070720−0234402	E	19.35	0.03	16.52	0.01	16.08	0.01	15.26	0.03	9.04	0.39
J14234238+3400324	S	15.37	0.02	13.97	0.01	13.77	0.01	13.36	0.02	0.09	1.22
J14234632+3401012	S	16.35	0.02	14.18	0.01	13.78	0.01	13.01	0.02	0.24	1.56
J14245831−0303597	S	17.81	0.02	15.85	0.01	15.50	0.01	14.90	0.44	0.24	1.26
J14245913−0304012	S	19.41	0.03	16.38	0.01	15.87	0.01	14.92	0.43	12.91	0.48
J14250552+0313590	E	17.84	0.02	15.28	0.01	14.90	0.01	14.07	0.01	0.88	1.27
J14250739+0313560	S	18.70	0.03	16.31	0.01	15.96	0.01	15.10	0.03	0.38	1.57
J14294766+3534275	S	17.10	0.02	14.42	0.01	14.00	0.01	13.25	0.02	5.03	0.49
J14295031+3534122	S	17.73	0.02	15.27	0.01	14.88	0.01	14.20	0.03	1.55	0.79
J14334683+4004512	S	17.29	0.02	14.71	0.01	14.27	0.01	13.37	0.01	0.69	1.45
J14334840+4005392	S	16.33	0.02	14.45	0.01	14.11	0.01	13.21	0.01	0.07	2.02
J14442055+1207429	S	17.28	0.02	15.11	0.01	14.74	0.01	13.96	0.02	0.22	1.62
J14442079+1207552	S	17.59	0.02	14.86	0.01	14.44	0.01	13.66	0.01	5.77	0.47
J15002374+4316559	E	17.60	0.02	14.88	0.01	14.45	0.01	13.62	0.01	3.06	0.81
J15002500+4317131	S	17.81	0.02	15.05	0.01	14.63	0.01	13.83	0.02	6.08	0.50
J15053137+3427534	S	18.98	0.03	16.36	0.01	16.01	0.01	15.47	0.02	13.00	0.00
J15053183+3427526	E	19.10	0.03	16.24	0.01	15.83	0.01	15.12	0.01	13.00	0.00
J15064391+0346364	S	17.56	0.02	14.90	0.01	14.50	0.01	13.71	0.01	2.88	0.76
J15064579+0346214	S	18.22	0.03	15.60	0.01	15.09	0.01	13.83	0.02	0.15	2.63
J15101587+5810425	S	17.59	0.02	15.08	0.01	14.70	0.01	14.03	0.10	2.42	0.63
J15101776+5810375	S	19.02	0.03	16.48	0.01	15.95	0.01	14.49	0.15	0.06	3.01
J15144544+0403587	S	18.35	0.03	15.49	0.01	15.03	0.01	14.17	0.01	7.48	0.53
J15144697+0403576	S	18.26	0.03	15.52	0.01	15.12	0.01	14.32	0.01	4.77	0.59
J15233768+3749030	S	17.57	0.02	15.37	0.01	15.04	0.01	14.51	0.06	0.82	0.77
J15233899+3748254	E	17.83	0.03	15.32	0.01	14.93	0.01	14.38	0.06	8.72	0.00
J15264774+5915464	S	18.55	0.03	15.74	0.01	15.33	0.01	14.58	0.03	13.00	0.04
J15264892+5915478	E	18.39	0.03	15.65	0.01	15.25	0.01	14.56	0.03	13.00	0.00
J15281276+4255474	S	16.40	0.02	13.89	0.01	13.42	0.01	12.30	0.01	0.18	2.29
J15281667+4256384	S	16.49	0.02	13.79	0.01	13.35	0.01	12.54	0.02	3.04	0.78
J15523258+4620180	E	18.97	0.03	16.05	0.01	15.63	0.01	14.91	0.02	13.00	0.00
J15523393+4620237	S	19.09	0.03	16.70	0.01	16.25	0.01	15.48	0.03	0.58	1.27
J15562191+4757172	S	17.47	0.02	15.30	0.01	14.93	0.01	14.21	0.07	0.31	1.37
J15562738+4757302	E	17.59	0.02	14.99	0.01	14.60	0.01	13.98	0.03	9.50	0.02
J15583749+3227379	S	19.11	0.03	16.48	0.01	16.05	0.01	15.23	0.03	1.49	1.07
J15583784+3227471	S	18.13	0.02	16.03	0.01	15.60	0.01	14.71	0.28	0.12	2.06
J16024254+4111499	S	16.97	0.02	15.38	0.01	15.09	0.01	14.34	0.10	0.05	1.69
J16024475+4111589	S	17.37	0.02	15.80	0.01	15.52	0.01	14.88	0.16	0.07	1.57
J16080559+2529091	S	18.95	0.03	15.91	0.01	15.37	0.01	14.24	0.02	2.26	1.45
J16080648+2529066	S	19.22	0.03	16.18	0.01	15.53	0.01	13.99	0.01	0.19	3.02
J16082261+2328459	S	19.14	0.03	16.92	0.01	16.53	0.01	15.84	0.05	0.43	1.23
J16082354+2328240	S	18.50	0.03	16.08	0.01	15.66	0.01	14.63	0.02	0.20	2.09
J16145418+3711064	S	18.74	0.03	15.85	0.01	15.41	0.01	14.53	0.02	8.17	0.53
J16145421+3711136	E	19.03	0.03	16.17	0.01	15.74	0.01	14.94	0.02	13.00	0.12
J16282497+4110064	S	17.88	0.02	15.25	0.01	14.85	0.01	14.23	0.02	12.99	0.00
J16282756+4109395	S	17.65	0.02	14.91	0.01	14.48	0.01	13.75	0.02	9.85	0.20
J16354293+2630494	S	19.36	0.03	16.44	0.01	15.97	0.01	15.18	0.04	13.00	0.00
J16354366+2630505	E	19.40	0.03	16.43	0.01	15.94	0.01	14.99	0.03	7.35	0.70
J16372583+4650161	S	19.11	0.03	16.19	0.01	15.72	0.01	14.70	0.04	2.52	1.21
J16372754+4650054	S	19.65	0.04	17.09	0.01	16.65	0.01	15.93	0.06	2.64	0.66
J17020320+1900006	E	19.30	0.03	16.17	0.01	15.70	0.01	14.94	0.02	13.00	0.00

Table 2
(Continued)

Name	Type	m_u (mag)	e_u (mag)	m_r (mag)	e_r (mag)	m_i (mag)	e_i (mag)	m_{K_s} (mag)	e_{K_s} (mag)	Age (Gyr)	A_v (mag)
(1)	(2)	(3)	(4)	(5)	(6)	(7)	(8)	(9)	(10)	(11)	(12)
J17020378+1859495	S	20.27	0.05	17.57	0.01	17.13	0.01	16.30	0.07	2.54	0.88
J17045089+3448530	S	18.90	0.03	16.73	0.01	16.26	0.01	15.30	0.10	0.11	2.18
J17045097+3449020	S	17.65	0.02	16.00	0.01	15.55	0.01	14.68	0.06	0.05	1.83
J20471908+0019150	S	15.73	0.02	12.82	0.01	12.34	0.01	11.49	0.04	12.15	0.33
J20472428+0018030	E	15.82	0.02	13.09	0.01	12.62	0.01	11.88	0.04	8.22	0.30

Note. The columns are: (1) galaxy name; (2) galaxy type, "S" for Spiral and "E" for Elliptical; (3), (5), (7), (9) 7 kpc aperture photometry result of *u*,*r*,*i* and K_s-band, respectively, and (4), (6), (8), (10) their errors; (11) stellar age generated from *u*-*r*-*i*-K_s color; (12) attenuation of *V*-band generated from *u*-*r*-*i*-K_s color.

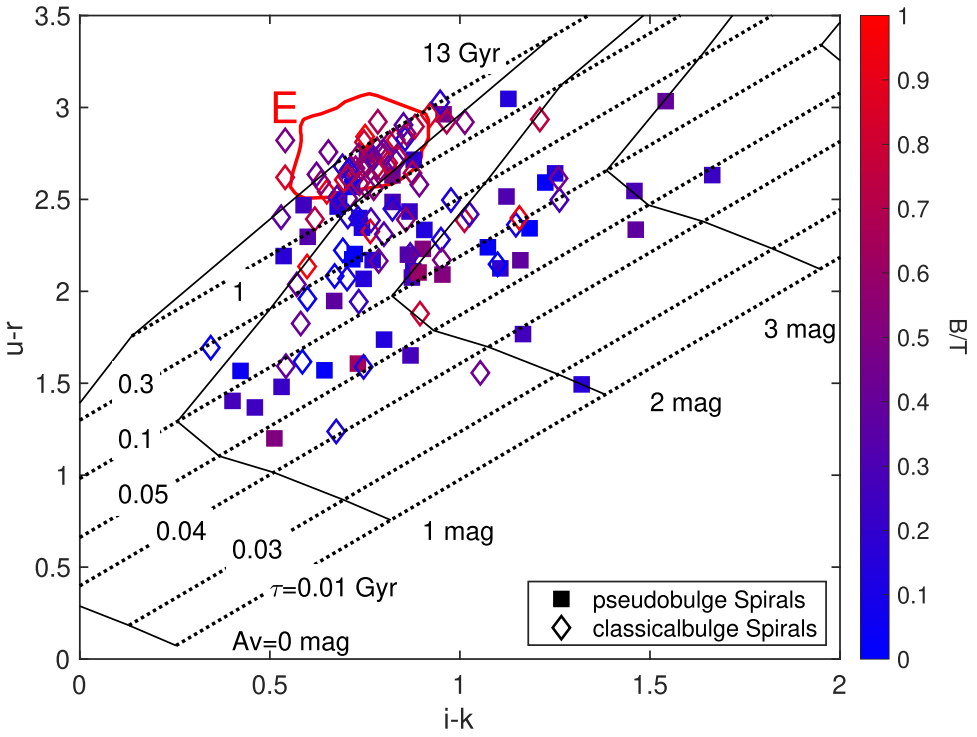

Figure 2. The *u*-*r*-*i*-K_s color–color diagram for Spirals with pseudobulges (filled squares) and classical bulges (open diamonds). The symbol color indicates the B/T ratio in He et al. (2022). The red contour delineates the region of the distribution of H-KPAIR elliptical galaxies. The mesh grid outlines the time after the instantaneous-burst τ (i.e., stellar age) and attenuation A_v in the model. From bottom to top the dotted lines are τ equal to 0.01, 0.03, 0.04, 0.05, 0.1, 0.3, 1, 13 Gyr, and from left to right the solid lines are A_v of 0, 1, 2, 3 mag.

populations with less star formation activity and dust attenuation. Indeed there are several galaxies with noticeable large classical bulge found to have high *Av*. We explain this by two aspects. First, these galaxies have high $sSFR_{enh}$, hence relatively high sSFR, though their control sample will have low sSFR. The SFR of the sample is derived from Herschel observation (Cao et al. 2016) and is mainly constrained by the dust temperature, then highly related to the attenuation. Second, our *u*-*r*-*i*-K_s color which generated the Av is of the central part of the galaxy instead of the whole galaxy, and old galaxies have dust gathering in the central region (or we can say bulge) is reasonable.

To investigate whether interaction can affect the bulge performance, we select a new control sample (control-sample-2 hereafter). The selection of control-sample-2 is similar to the control sample in (He et al. 2022, Section 4) except for without

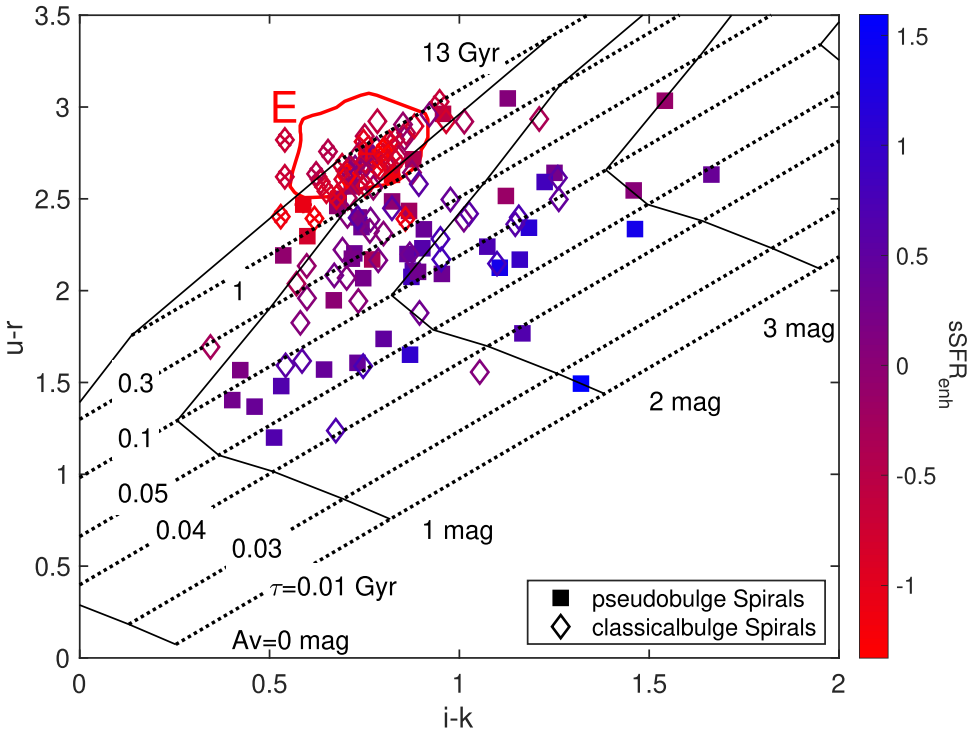

Figure 3. Same *u-r-i-K*$_s$ color–color diagram as Figure 2, but the color indicates the sSFR$_{enh}$. The data points marked by crosses are SFR undetected in Cao et al. (2016).

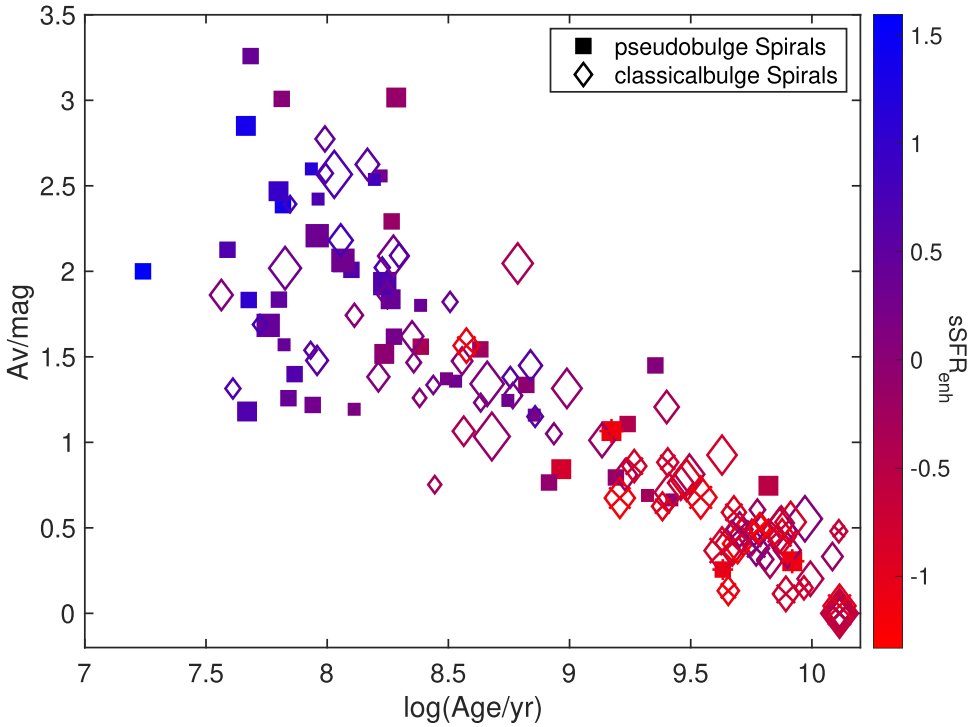

Figure 4. Plot of the attenuation A_v vs. age of the central stellar population for all spiral galaxies in the H-KPAIR. The color of symbols represents the sSFR$_{enh}$, and the size of symbols represents the B/T ratio. The filled squares and the open diamonds represent pseudobulge galaxies and classical galaxies, respectively. The data points marked by crosses are SFR undetected in Cao et al. (2016).

matching the B/T. The criteria of control-sample-2 go as follows:

1. Should be identified as a spiral in galaxy Zoo (Lintott et al. 2008).
2. Not in any interacting system, namely no neighbor galaxy in the SDSS database which has projected distance $\leqslant$100 kpc and observed redshift difference $\leqslant$1000 km s^{-1}.
3. Has reliable B/T ratio, namely having $\chi^2/\nu < 2$ and no bad flag (flag bit 20 = 0) in Meert et al. (2015).
4. The L_K matches that of the paired galaxy within 0.1 dex.
5. Match of local density: we adopt a local density indicator $N_{1\mathrm{Mpc}}$, which is the count of galaxies brighter than $M_r = -19.5$ and with redshifts differing less than 1000 km s^{-1} from that of the target galaxy, in the surrounding sky area of radius = 1 Mpc (the count includes the target galaxy itself if it is brighter than $M_r = -19.5$). By means of $N_{1\mathrm{Mpc}}$, we classify galaxies into four environmental categories: field ($N_{1\mathrm{Mpc}} \leqslant 3$), small group ($4 \leqslant N_{1\mathrm{Mpc}} \leqslant 6$), large group ($7 \leqslant N_{1\mathrm{Mpc}} \leqslant 10$), and cluster ($N_{1\mathrm{Mpc}} > 10$). The control galaxy will be in the same environmental category as the paired galaxy.
6. Has the closest redshift, among all qualified candidates, to that of the paired galaxy.

In Figure 5 we compare the Age and B/T ratio of the paired galaxies which are separated into two subsamples: (1) galaxies with pseudobulges and (2) those with classical bulges. Also plotted are the means of the Age for Spirals in H-KPAIR/control-sample-2 with error bars in the five B/T bins for the two subsamples: (1) $B/T \leqslant 0.1$, (2) $0.1 < B/T \leqslant 0.3$, (3) $0.3 < B/T \leqslant 0.5$, (4) $0.5 < B/T \leqslant 0.7$, (5) $B/T > 0.7$. It shows that, on average, the Age of the central stellar population of galaxies with classical bulges increases with the B/T ratio. This is indeed anticipated because the dominance of the bulge to central colors increases with the B/T ratio (Figure 1), and in general stellar populations in classical bulges are older than those in disks (Driver et al. 2006; Kim et al. 2016). In contrast, for galaxies with pseudobulges, the Age of central stellar populations is rather flat against the B/T ratio, namely the stellar populations have about the same Ages as those in the inner disks of the disky galaxies (with $B/T \sim 0$). This confirms that pseudobulges are different from classical bulges, and the former are dominated by the "disk phenomena" such as bars and nuclear disks/rings as assumed in He et al. (2022). However, some individual galaxies with pseudobulges have central stellar populations with old Ages of >1 Gyr. Their pseudobulges are unlikely related to any central star formation activity, as indicated by the low star formation enhancement ($\mathrm{sSFR_{enh}} \lesssim 0$). They have relatively low B/T ratios (most with $B/T < 0.3$, all with $B/T < 0.5$) and may be similar to those single late-type galaxies with relatively small pseudobulges found in Kim et al. (2016).

It is also interesting to note that a few galaxies with large classical bulges are located in the lower-right quadrant of Figure 5, namely their central stellar populations appear to have relatively young Ages. They may contain starbursts or post-starbursts in the central region which can outshine the old stellar populations and make the bulges "blue." An outstanding example of these galaxies is J13151726+4424255, which has a classical bulge with B/T = 0.94, Age = 0.11 Gyr, and $\mathrm{sSFR_{enh}} = 0.70$. Compared to galaxies in the control sample, paired galaxies with large bulges, particularly those in the forth bin of the B/T ratio ($0.5 < B/T \leqslant 0.7$), have higher Ages. Individual inspections of these galaxies indicate that most of them have elliptical companions (i.e., in SE pairs). Their star formation history might have been affected by the environment associated with the Ellipticals (see the discussion in Section 5).

Figures 6 and 7 show the possibility density function (pdf) of classical bulges and pseudobulges in the five bins for SFGs in H-KPAIR and control-sample-2, respectively. The paired Spirals have lower fraction of pure disk galaxies (bin1, $B/T \leqslant 0.1$), we attribute this to some paired disky galaxies having nuclear/circum-nuclear starburst and their B/T ratio raising to higher B/T bins. Nevertheless, these galaxies have a flat profile and are identified as pseudobulge galaxies and are assigned B/T = 0 in He et al. (2022)

4.2. Paired SFGs with Strong Enhancement

In Section 2 we defined SFGs by $\log(\mathrm{sSFR}/\mathrm{yr}^{-1}) \geqslant -11.3$ (see also Cao et al. 2016; He et al. 2022). Most of the non-SFGs are SFR undetected (marked by crosses in Figures 2, 4 and 5) in Cao et al. (2016), and they are mostly early-type galaxies with large old classical bulges. Taking these galaxies into the $\mathrm{sSFR_{enh}}$ analysis will not affect our results. From now on we focus on the SFGs subsample.

Figure 8 is a plot of $\mathrm{sSFR_{enh}}$ against B/T ratio, which is similar to Figure 9 of He et al. (2022) except for using the original B/T values (instead of B/T = 0) for galaxies with pseudobulges, and the five bins are divided the same as in Figure 5. It shows a broad scatter of $\mathrm{sSFR_{enh}}$ for galaxies with pseudobulges, which spans about two orders of magnitude (~1 orders magnitude larger than that for galaxies with classical bulges). This demonstrates that the broad scatter of $\mathrm{sSFR_{enh}}$ for disky galaxies (with $B/T < 0.1$) found by He et al. (2022) is indeed due to galaxies with pseudobulges which are assigned B/T = 0 in that paper. The mean $\mathrm{sSFR_{enh}}$ of pseudobulge SFGs is rather constant against the B/T ratio, in contrast to that of SFGs with classical bulges which decreases with increasing B/T (Figure 8; see also He et al. 2022). The mean $\mathrm{sSFR_{enh}}$ of SFGs with pseudobulges ($\mathrm{sSFR_{enh}} = 0.33 \pm 0.07$) is higher than that of SFGs with classical bulges ($\mathrm{sSFR_{enh}} = 0.12 \pm 0.06$) at 2σ level.

The eight SFGs with the highest $\mathrm{sSFR_{enh}}$ all have pseudobulges (Figure 8). In order to study the galaxies with the strong sSFR enhancement in detail, we concentrate on those

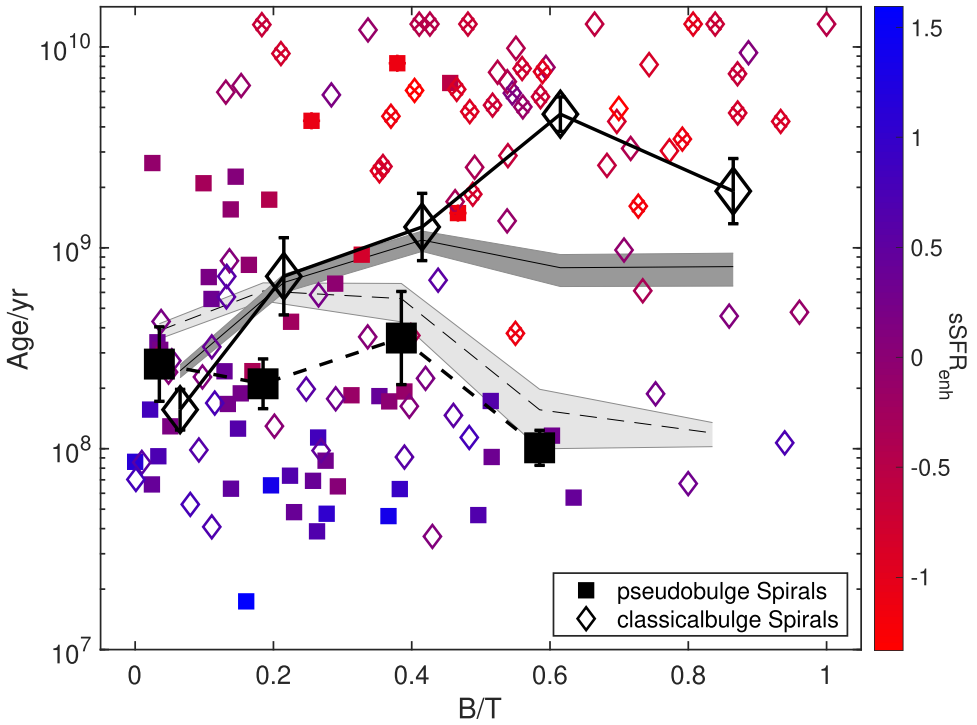

Figure 5. Plot of Age vs. B/T ratio for Spirals with pseudobulges (small filled squares) and with classical bulges (small open diamonds). The color of symbols represents $sSFR_{enh}$. The large black squares and large black diamonds represent the means of pseudobulge galaxies and of classical-bulge galaxies in the five B/T ratio bins, respectively. The error bars show the 1σ errors of the means. The lines with light and dark shaded areas represent the means and their errors of the two kinds of galaxies in control-sample-2. The data points marked by crosses are SFR undetected in Cao et al. (2016).

having $sSFR_{enh} > 0.7$, corresponding to more than 5 times sSFR enhancement compared with the median of the matching controls. With this criterion, there are 13 strongly enhanced SFGs in our sample, nine with pseudobulges and four with classical bulges (see Figure 8 and Table 3). Figure 9 shows that their central stellar populations all have Ages younger than 200 Myr, namely are dominated by stars formed recently. Excluding these galaxies, the rest of our sample have a mean $sSFR_{enh} = 0.11 \pm 0.04$, which is only marginally significant at 2.8σ level. Statistically, SFGs with strong enhancement represent 13% (=13/98) of SFGs in our sample and 10% (=13/132) of all spiral galaxies in the H-KPAIR sample.

Seven of the 13 galaxies with strong enhancement have Spitzer observations and consequently, the 8 μm flux densities of both the nuclear emission (aperture size: D = 4 kpc) and the total emission (Xu et al. 2010). In Figure 10 we plot $sSFR_{enh}$ against $C_{8\mu m}$ for these galaxies, where $C_{8\mu m}=f_{8\mu m,nuclear}/f_{8\mu m,total}$ is the nuclear-to-total ratio of the 8μm emission. $C_{8\mu m}$ is an indicator of the nuclear concentration of star formation in a galaxy. The plot shows a significant linear correlation between $sSFR_{enh}$ and $C_{8\mu m}$ (the Pearson's linear correlation coefficient $r_P = 0.81$ and the significance $p_P = 0.03$) for these galaxies. Among the seven SFGs in the plot, all the five with pseudobulges have relatively high nuclear concentration ($C_{8\mu m} \geqslant 0.49$) whereas, for the two SFGs with classical bulges, the star formation occurs mostly outside the nuclear region ($C_{8\mu m} < 0.30$). Albeit the small sample size, the plot indicates that the pseudobulges in galaxies with strong enhancement are tightly related to nuclear/circum-nuclear starbursts. Given that most galaxies with strong enhancement have pseudobulges, our result suggests that nuclear/circum-nuclear starburst may be the dominant mode for strong tidally induced star formation in paired galaxies. On the other hand, for a low fraction of paired SFGs (particularly those with classical bulges), the tidally induced star formation may be widely distributed over the entire disk. These results are consistent with the literature which shows that nuclear/circum-nuclear starbursts are common among paired galaxies with strong signs of interaction while wider spread star formation enhancement is also observed in some of them (Keel et al. 1985; Kennicutt et al. 1987; Pan et al. 2019; Steffen et al. 2021).

Figures 11 and 12 are optical (u, g, r) color images of the nine pseudobulge galaxies with strong enhancement and four classical-bulge galaxies with strong enhancement, respectively. These images are taken from the database of Dark Energy Spectroscopic Instrument (DESI[12]) which are deeper and of

[12] https://www.legacysurvey.org/

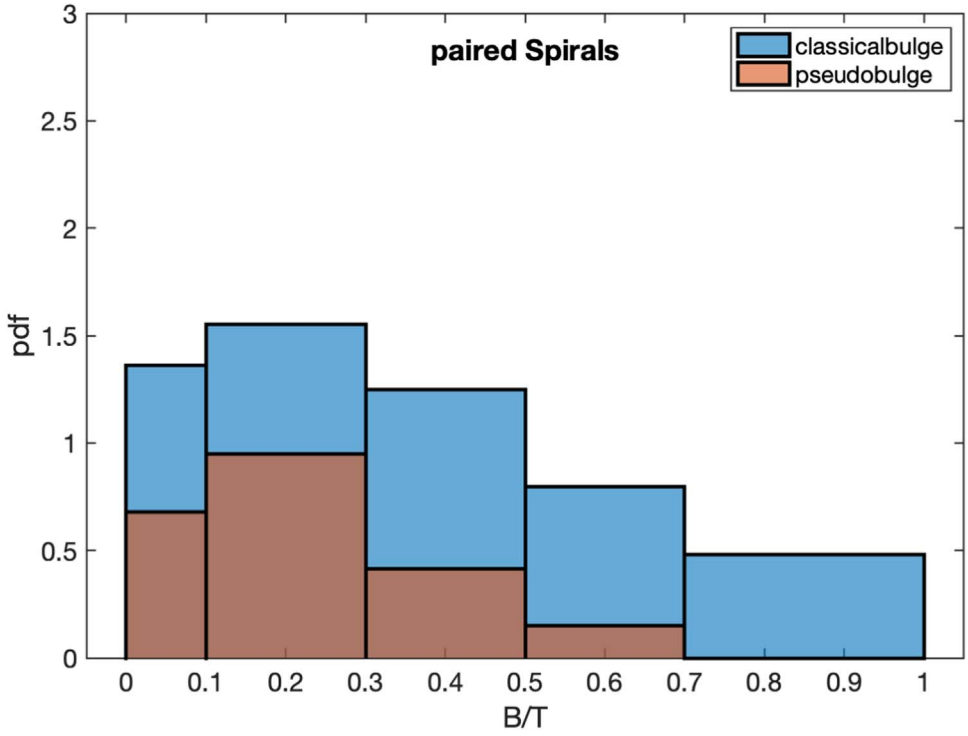

Figure 6. Probability density function of pseudobulge Spirals and classical bulge Spirals in H-KPAIR.

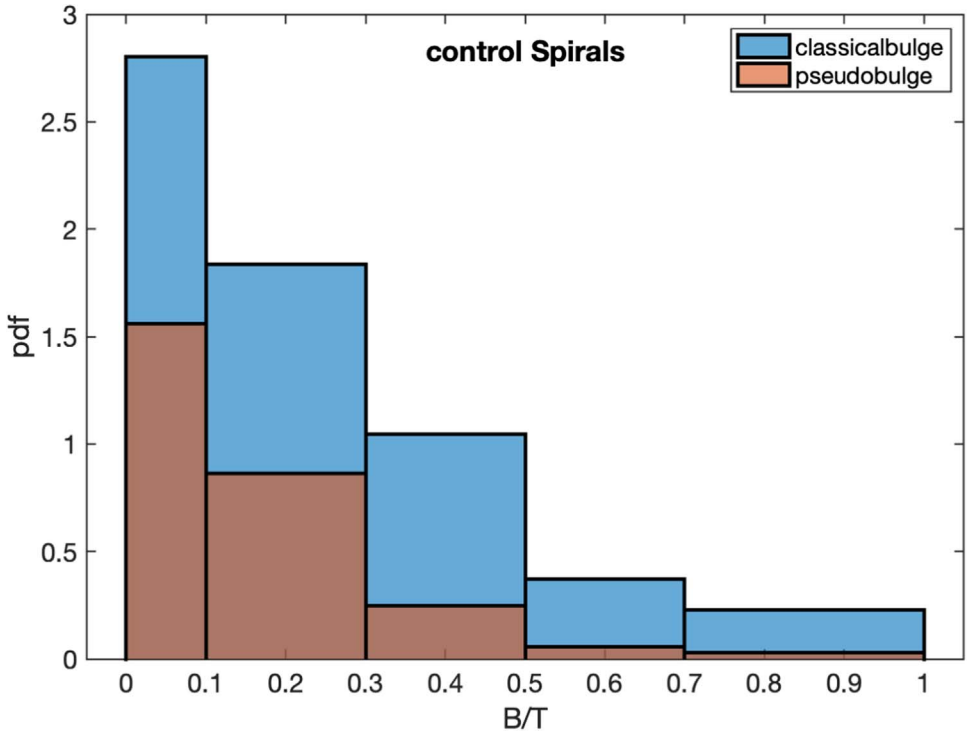

Figure 7. Probability density function of pseudobulge Spirals and classical bulge Spirals in control-sample-2.

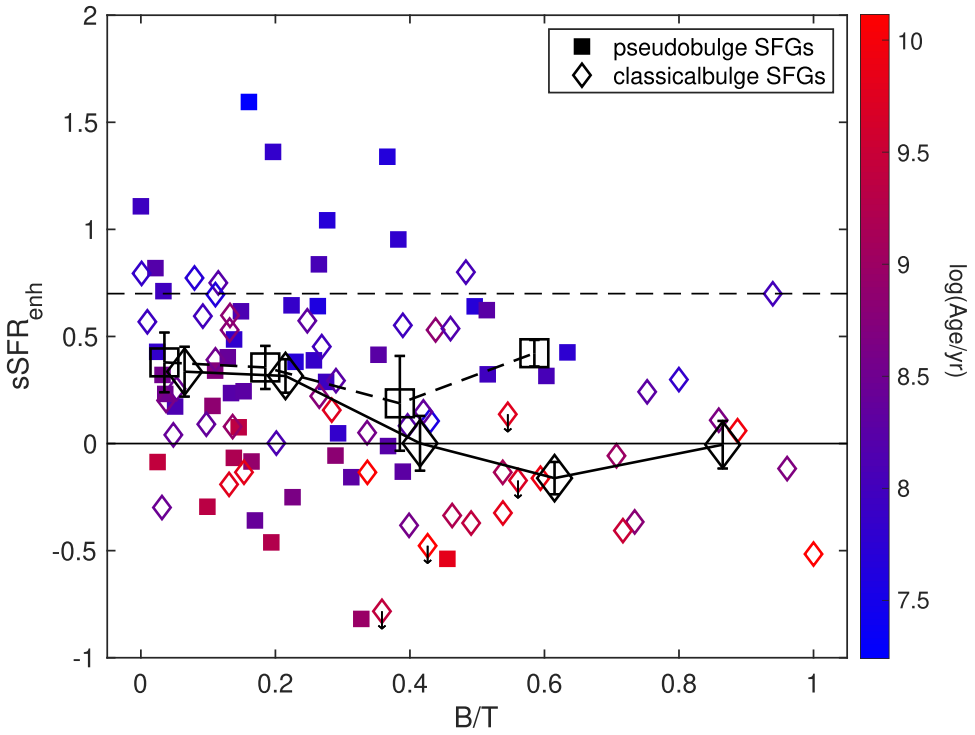

Figure 8. Plot of $sSFR_{enh}$ vs. B/T ratio for SFGs with pseudobulges (small filled squares) and SFGs with classical bulges (small open diamonds). The color of symbols represents the Age of the central stellar population. The large black open squares and large black open diamonds represent the means of pseudobulge galaxies and of classical-bulge galaxies in the five B/T ratio bins, respectively. The error bars show the 1σ errors of the means. The horizontal solid line and dashed line mark $sSFR_{enh} = 0$ and $sSFR_{enh} = 0.7$, respectively.

better angular resolutions than SDSS images and therefore can show the diffuse features more clearly. Four pseudobulge galaxies J07543194+1648214, J09155467+4419510, J09155552+4419580, and J17045097+3449020 (panels (b), (c), (g) of Figure 11) and two classical-bulge galaxies J10100079+5440198 and J17045089+3448530 (panels (b), (d) of Figure 12) are found in pairs seemed to be almost coalesced, namely in a late merging stage. This result suggests that a high fraction ($6/13 = 46\%$) of galaxies with strong enhancement are in late-stage mergers. Here we separate late-stage mergers (pairs with strong interaction signs and very close nuclei) from early-stage mergers (pairs without strong interaction signs or the two galaxies being widely separated). The late-stage mergers are likely seen during or after the second close encounter, because it takes relatively long time (more than a few 100 Myr) for galaxies to develop the interaction features after the first close encounter. In general, only a low fraction of paired galaxies selected in optical and/or near-IR bands (such as H-KPAIR) are late-stage mergers because this stage lasts significantly shorter than the stage before it (Di Matteo et al. 2007). Also, for the H-KPAIR sample, the selection criterion of separation $\geqslant 5\,h^{-1}$ kpc excludes some late-stage mergers, particularly those which are already coalesced. Hence, the fact that in our sample late-stage mergers represent 46% of SFGs with strong enhancement suggests that the majority of SFGs in late-stage mergers may harbor strong tidally induced star formation whereas only a very low fraction of SFGs in early-stage mergers may do so. For the latter, significant SFR enhancement may be triggered by strong tidal torques only in SFGs that are undergoing or passed the first close encounter (namely pericenter passage in Feng et al. 2020) in low-speed coplanar orbits (namely with well spin–orbit alignment in Moon et al. 2021) as argued by Xu et al. (2021).

The remaining seven galaxies with strong enhancement are in earlier-stage mergers with the two component galaxies clearly separated. Among them, J01183414-0013417, J13153506+6207286, and J16024257+4111501 (panels (a), (e) of Figure 11 and panel (c) of Figure 12) are likely in interaction systems with low-inclination orbits and low orbital velocity (all having $\delta v < 70\,km\,s^{-1}$ where δv is the measured relative radial velocity of the companion). Particularly J13153506+6207286 (panel (e) of Figure 11), which is in Arp 238 ($\delta v = 6\,km\,s^{-1}$), has been confirmed to have a coplanar orbit by a simulation of Holincheck et al. (2016). Xu et al. (2021) found a very compact molecular gas concentration in its nucleus which is fueling a strong active nuclear starburst. They argued that the nuclear starburst is triggered by a strong tidal torque which has been predicted by simulations for galaxies in low-speed coplanar

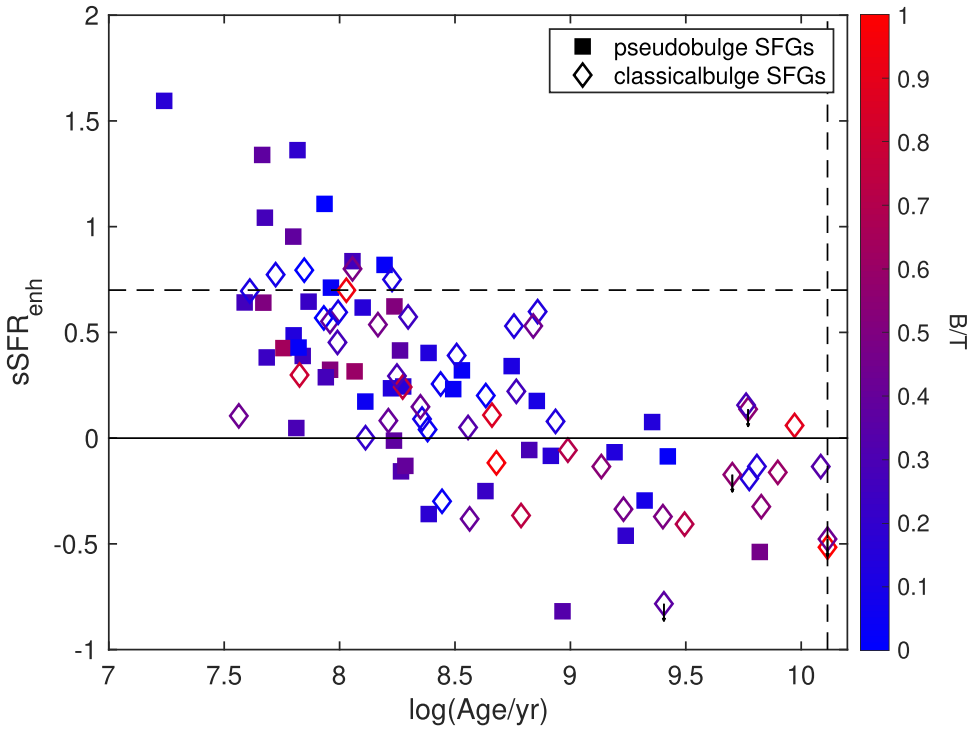

Figure 9. Plot of $sSFR_{enh}$ vs. age of the central stellar population SFGs with pseudobulges (filled squares) and SFGs with classical bulges (open diamonds). The color of symbols represents the B/T ratio. The horizontal solid line and dashed line mark $sSFR_{enh} = 0$ and $sSFR_{enh} = 0.7$, respectively.

Table 3
SFGs with Strong Enhancement

Name	z	$sSFR_{enh}$ (dex)	pair_type	bulge_type	merge_stage	δv (km s^{-1})	$\log M_{HI+H2}$ ($M_\odot$)	$f_{8\mu m,nulear}$ (mJy)	$f_{8\mu m,total}$ (mJy)
(1)	(2)	(3)	(4)	(5)	(6)	(7)	(8)	(9)	(10)
J01183417−0013416	0.0453	1.34	SS	p	early	54	10.45	33.67	57.06
J03381222+0110088	0.0392	0.75	SE	c	early	432.9	10.45	…	…
J07543194+1648214	0.0459	0.71	SS	p	late	104.1	10.09	…	…
J09155467+4419510	0.0396	1.11	SS	p	late	2.4	…	…	…
J09155552+4419580	0.0396	1.36	SS	p	late	2.4	…	…	…
J10100079+5440198	0.0460	0.79	SS	c	late	83.7	…	179.52	187
J10332972+4404342	0.0523	0.84	SS	p	early	64.2	…	26.13	49.3
J13153506+6207287	0.0306	1.59	SS	p	early	6	10.05	39.86	55.36
J14005783+4251203	0.0327	0.82	SS	p	early	234.3	10.05	23.52	47.99
J14005879+4250427	0.0335	0.95	SS	p	early	234.3	9.88	…	…
J16024254+4111499	0.0335	0.77	SS	c	early	69	10.38	…	…
J17045089+3448530	0.0572	0.80	SS	c	late	270	…	22.49	77.56
J17045097+3449020	0.0563	1.04	SS	p	late	270	…	4.61	15.88

Note. The columns are: (1) galaxy name; (2) redshift; (3) specific star formation rate enhancement; (4) pair type: "SS" for Spiral+Spiral pair, "SE" for Spiral +Elliptical pair; (5) bulge type: "p" for pseudo-bulge, "c" for classical-bulge; (6) interaction type (detailed description in Cao et al. 2016); (7) difference in radial velocity between two galaxies in a pair; (8) HI gas mass in Zuo et al. (2018) plus H_2 gas mass in Lisenfeld et al. (2019), where the HI mass is divided by M_{star} ratio for SS pairs, and all assigned to the spiral for SE pairs; (9) Spitzer 8μm flux of the galaxy nuclear region (Xu et al. 2010); (10) Spitzer 8μm flux of the total galaxy.

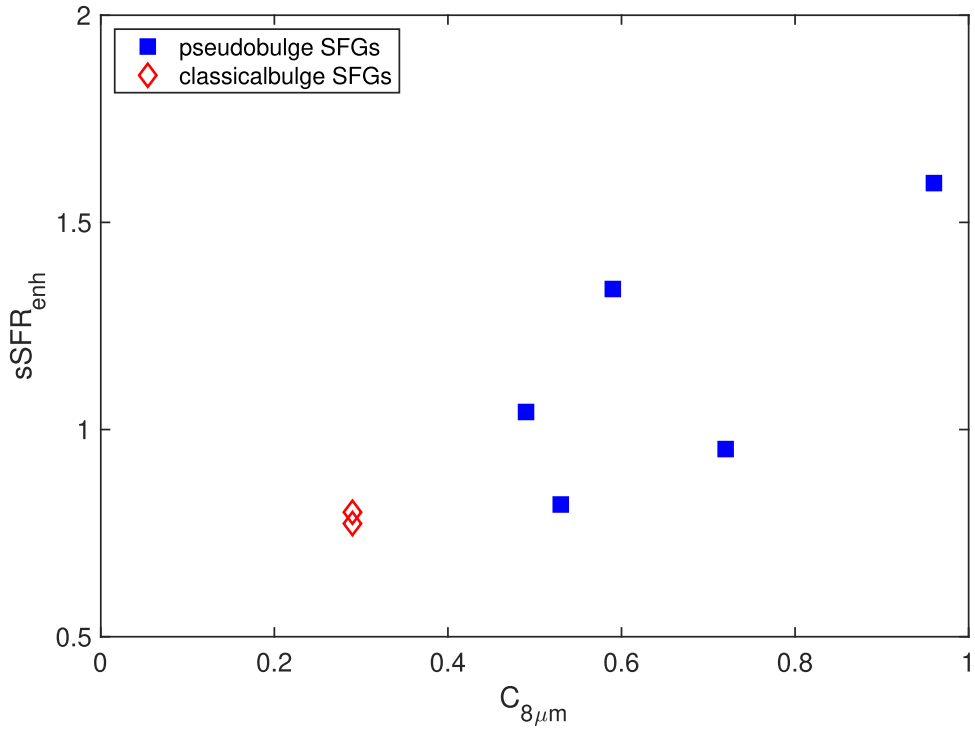

Figure 10. Plot of $sSFR_{enh}$ vs. the nuclear-to-total ratio of the 8μm emission $C_{8\mu m}$.

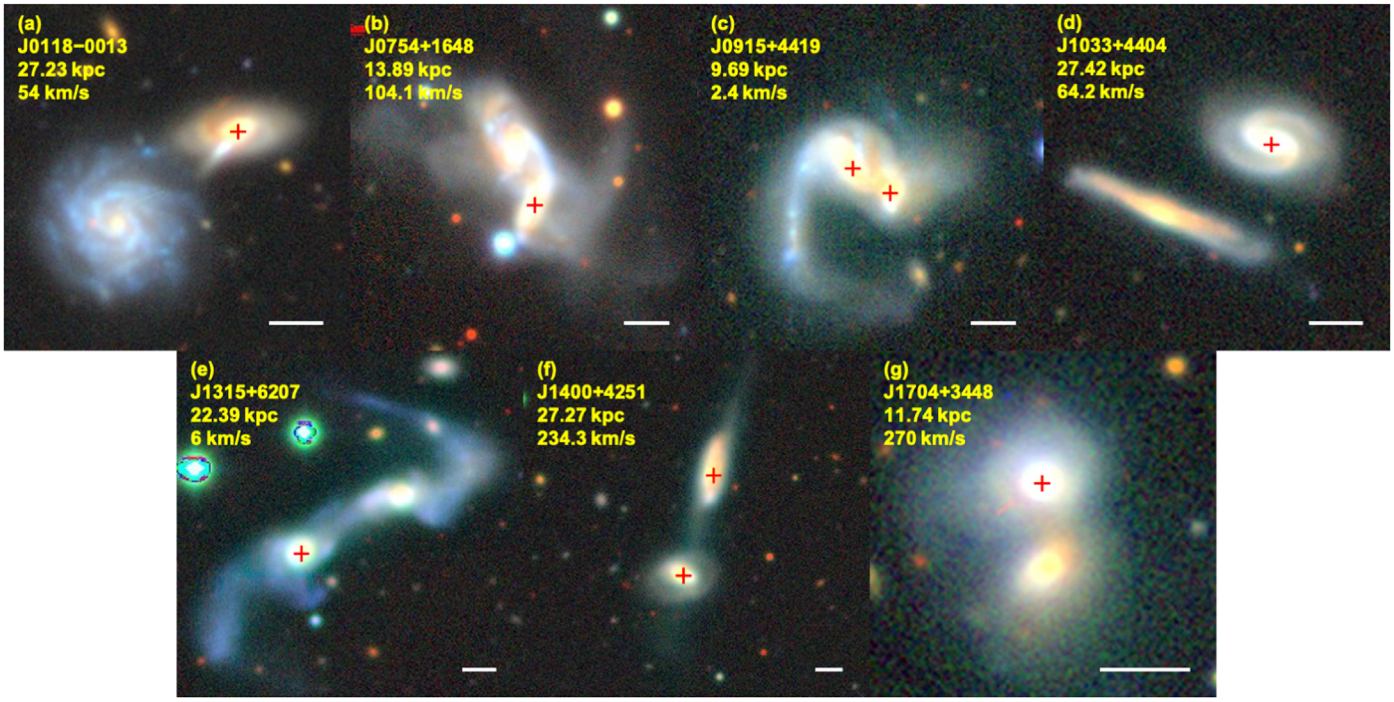

Figure 11. Dark Energy Spectroscopic Instrument (DESI) images of nine pseudobulge galaxies with strong star formation enhancement. The strongly enhanced galaxies are marked by red plus signs. The white dash on the bottom-right corner of each stamp illustrates the angular scale of 10″. The pair projected separation and radial velocity difference are provided as well.

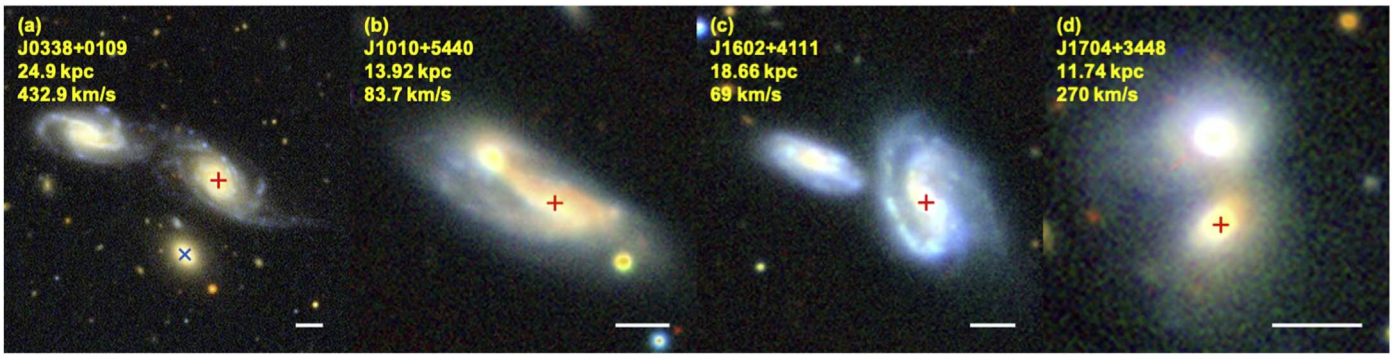

Figure 12. DESI images of four classical bulge galaxies with strong star formation enhancement. The red plus signs mark the strongly enhanced galaxies. The blue cross in the image of J0338+0109 marks the E component of the pair. The white dash on the bottom-right corner of each stamp illustrates the angular scale of 10″. The pair projected separation and radial velocity difference are provided as well.

interactions (Barnes & Hernquist 1996; Hopkins et al. 2009). This interpretation may also apply to J01183414-0013417 and J16024257+4111501. In contrast, J10332972+4404342, J140 05783+4251203, and J14005879+4250427 (panels (d), (f) of Figure 11) may be in high-inclination orbits, and the latter two are members of the same pair (KPAIR J1400+4251) which has a high relative radial velocity ($\delta v = 234\,\mathrm{km\,s^{-1}}$). These three galaxies all have pseudobulges and might be bar galaxies from the appearance though it is uncertain given the limited resolution of the images. If this is true then their central starbursts may be field by the bars. Finally, J03381222 +0110088 (panel (a) of Figure 12) is the only one that is in an S+E pair among the 13 SFGs with strong enhancement. However, as shown in the optical image, it appears to be interacting with another nearby SFG which is in the same group of the S+E pair. The three galaxies form a close triplet dominated by SFGs. Therefore J03381222+0110088 is not in a de facto S+E pair. It has a very high total gas content with $M_{\mathrm{H_2}+HI}/M_{\mathrm{star}} = 0.56$ and a relatively low star formation efficiency of $\mathrm{SFE} = \mathrm{SFR}/M_{\mathrm{H_2}} = 10^{-9.10}\,\mathrm{yr^{-1}}$, which is below the average SFE of the H-KPAIR sample in Lisenfeld et al. (2019). It appears that the high sSFR of J03381222+0110088 is mainly due to its very high gas content which may not be related to any tidal effect.

4.3. Pseudo-bulge Galaxies in S+S and S+E Pairs

In their study of the B/T dependence of $\mathrm{sSFR_{enh}}$, He et al. (2022) found that except for in the last bin of $0.5 < \mathrm{B/T} \leqslant 1$ where SFGs in S+S and S+E pairs have similar means of $\mathrm{sSFR_{enh}}$ (both consistent with $\mathrm{sSFR_{enh}} = 0$), in all other B/T bins the former have higher $\mathrm{sSFR_{enh}}$ means than the latter. Particularly in the lowest bin of $\mathrm{B/T} \leqslant 0.1$, the difference is 0.4 ± 0.1 dex. In He et al. (2022) pseudobulge galaxies are assigned with the same $\mathrm{B/T} = 0$ and therefore are included in the bin $\mathrm{B/T} \leqslant 0.1$. Do pseudobulge SFGs in S+S and in S+E pairs have significantly different $\mathrm{sSFR_{enh}}$?

In Figure 13 we compare pseudobulge SFGs in S+S pairs and in S+E pairs. It plots $\mathrm{sSFR_{enh}}$ against the stellar mass M_{star}, with the color scale indicating the Age and the symbol size the B/T ratio. The plot shows clearly that, compared to pseudobulge SFGs in S+S pairs, those in S+E pairs tend to have older stellar populations and lower sSFR enhancements and none has strong enhancement ($\mathrm{sSFR_{enh}} \geqslant 0.7$). The means of $\mathrm{sSFR_{enh}}$ are 0.45 ± 0.08 and -0.04 ± 0.11 for pseudobulge SFGs in S+S pairs and in S+E pairs, respectively, and the difference is above 3σ. Most of the pseudobulge SFGs in S+E pairs (9 of 11) have relatively low stellar mass ($\leqslant 10^{10.6}\,M_{\odot}$).

Figure 14 compares pseudobulge SFGs in S+S and S+E in a plot of $\mathrm{sSFR_{enh}}$ versus the local density indicator N_{1Mpc} (defined in He et al. 2022 and also introduced in Section 4.1). SFGs in high-density regions with $\mathrm{N_{1Mpc}} \geqslant 7$ have significantly lower $\mathrm{sSFR_{enh}}$ than the rest of the sample, and a higher fraction (5/11) of pseudobulge SFGs in S+E, compared to those in S +S, are in this category. These SFGs should be in rich groups/ clusters, where star formation may be quenched by galaxy harassment (Moore et al. 1998) and/or ram pressure stripping (Gunn et al. 1972; Giovanelli & Haynes 1983; Gavazzi et al. 2006). Also, these paired SFGs may have very low probability of being in a coplanar orbit because of the frequent disturbance and therefore are less likely to have nuclear starbursts (Xu et al. 2021). Detailed inspections of the optical images show that their pseudobulges often correspond to bars or inner rings with low star formation activity (for example J12191866+1201054 which has $\mathrm{sSFR_{enh}} = -0.01$, Figure 15).

The mean and errors of H_2 gas mass fraction (Lisenfeld et al. 2019) and those of the total gas mass derived from FIR dust mass (Cao et al. 2016) were plotted in two B/T bins: (1) disk dominant ($\mathrm{B/T} \leqslant 0.3$), (2) bulge dominant ($\mathrm{B/T} > 0.3$) in Figures 16 and 17, as well the SFE calculated from them in Figures 18 and 19, separately. Generally, there is a decreasing sign for both H_2 gas and the total gas on B/T. The pseudobulge SFGs in S+S pairs have the most flat slope, while they have the

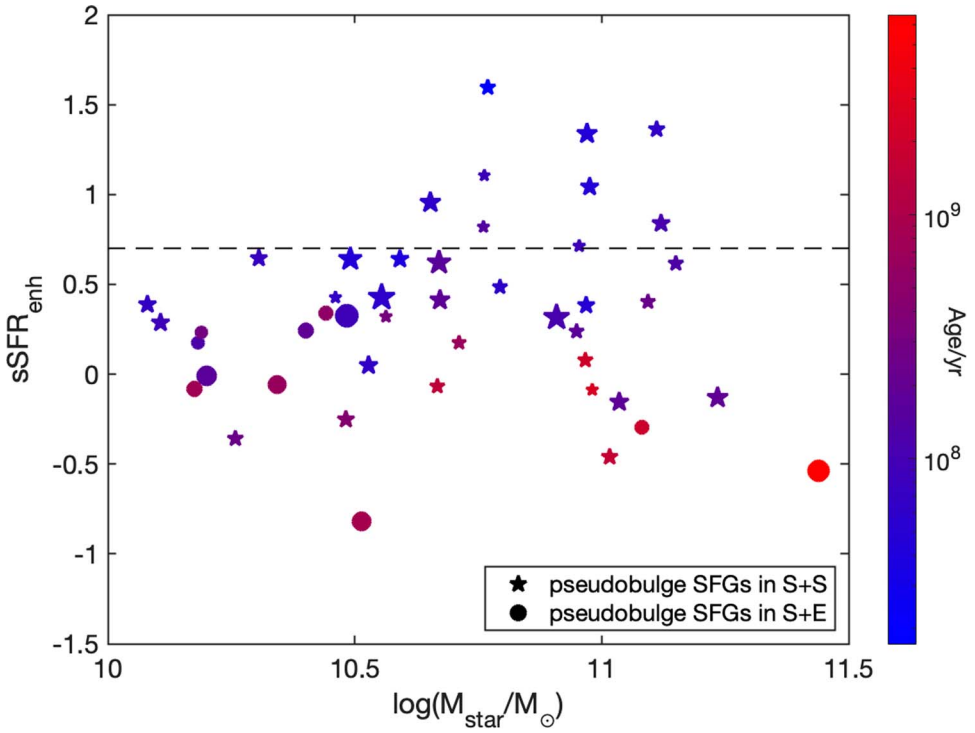

Figure 13. Plot of $sSFR_{enh}$ vs. $\log(M_{star})$ for pseudo-bulge SFGs in S+S pairs (pentagram) and in S+E pairs (circle). The symbol color indicates the Age of the central stellar population, and the symbol size shows the B/T ratio. The dashed line corresponds to $sSFR_{enh} = 0.7$.

highest gas fractions in bulge dominant galaxy (bin 2). No obvious trend is found in either SFE versus B/T. When comparing the subsamples, the pseudobulge SFGs have higher SFE_{gas}, and the SFGs in S+S pairs take the lead in both SFE. The most attractive point is that the pseudobulge galaxies in S+E pairs have not as high SFE as the classical bulge galaxies in S+S pairs.

5. Discussion

The significant sSFR enhancement of close major-merger pairs is mainly due to a small population of SFGs with strong enhancement (~15% in our sample; Figure 8). About half of these SFGs are found in late-stage mergers, all of which are in S+S pairs and none in an S+E pair. It is unlikely that any of the late-stage S+S mergers containing strong enhanced SFGs can be misclassified S+E mergers because none of the galaxies in these pairs is dominated by a classical bulge (the largest classical bulge is found in J17045088+3448529 shown in panel (d) of Figure 12 with a $B/T = 0.48$).

What is the reason for spirals in late-stage S+E mergers to avoid strong starbursts? There are four S+E late-stage mergers in H-KPAIR, which are listed in Table 4. Each of them has the two member galaxies nearly coalesced within a common halo (Figure 20). They are pairs of massive galaxies with the primaries more massive than $10^{11}/M_{\odot}$. All spiral galaxies in these pairs are rather quiescent in star formation and only one of them (J16354293+2630494; panel (d)) is included in our SFG sample with an $sSFR = 10^{-11.26}\,yr^{-1}$. They are uniformly gas-poor with the M_{gas}/M_{star} ratio less than 4% (Cao et al. 2016). which is lower than the ratios of 88% of SFGs in the H-KPAIR sample, and significantly below the mean of the sample ($M_{gas}/M_{star} = 0.13 \pm 0.01$).

Three galaxies J10514450+5101303, J13131470+3910382, and J16354293+2630494 (panel (a), (c) and (d) of Figure 20) are in pairs containing the most massive galaxies of rich groups or clusters that have more than 12 members (Yang et al. 2012). For them, the rich-group/cluster environment may be the key to the lack of cold gas and star formation because the ram pressure stripping and/or evaporation by the hot gas in IGM can remove most of the cold gas in the ISM and tidal tails. J11542299+4932509 (panel (b) of Figure 20) is apparently in an isolated pair. Its companion (J11542307+4932456) is a very massive Elliptical with $M_{star} = 10^{11.35}\,M_{\odot}$. The pair is detected by ROSAT in X-ray with a flux of $f_{0.2\text{–}2\,keV} = 8.22(\pm 1.73) \times 10^{-14}\,erg\,s^{-1}\,cm^{-2}$. This may be indicative of the presence of a hot gas halo around the pair which can strip/evaporate the cold gas and be responsible for the low gas content ($M_{gas}/M_{star} = 0.035$) and low sSFR ($<10^{-11.33}\,yr^{-1}$) of J11542299+4932509.

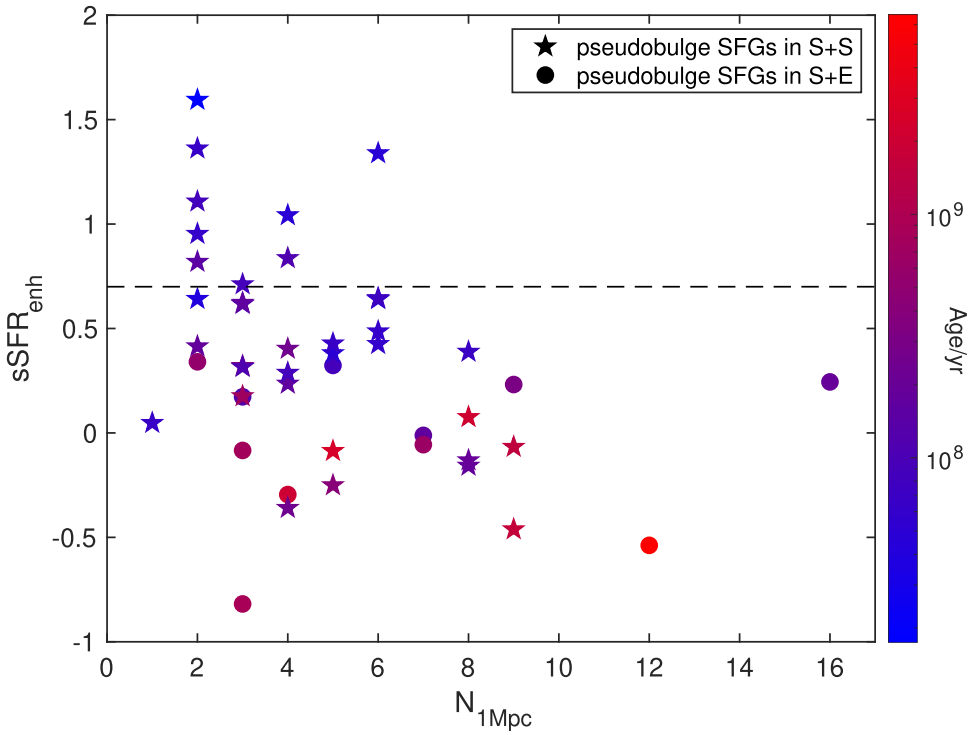

Figure 14. Plot of $sSFR_{enh}$ vs. N_{1Mpc}, where N_{1Mpc} is an indicator of local density defined by the number of galaxies brighter than $M_r = -19.7$ mag within 1 Mpc projected distance around the galaxy in question (He et al. 2022). Filled pentagrams and filled circles represent pseudobulge SFGs in S+S pairs and in S+E pairs, respectively. The dashed line corresponds to $sSFR_{enh} = 0.7$.

Thus, it appears that the lack of strong enhancement in late-stage S+E mergers may be due to the removal of cold gas by hot gas in the immediate environment (Park & Choi 2009; Hwang et al. 2011). It should be pointed out that the quiescent spiral galaxies in these late-stage S+E pairs are different from the SFGs studied by Cao et al. (2016) and Lisenfeld et al. (2019). These authors found no significant difference in M_{gas}/M_{star} and in M_{H_2+HI}/M_{star} between SFGs in S+S and S+E pairs, and therefore refuted the "cold-gas stripping" hypothesis as far as SFGs in S+E pairs are concerned. A majority of spirals in S+E pairs are SFGs ($64\% = 28/44$ for H-KPAIR), and many of them are gas-rich (e.g., NGC 2936 in Arp 142; Xu et al. 2021). It will be interesting to find out why they are absent in late-stage S+E mergers.

The interaction-induced star formation enhancement is affected by many factors, some seem to be necessary conditions (e.g., a galaxy should have gas to fuel star formation), but it is hard to say which is a sufficient condition. For instance, the four most enhanced classical bulge SFGs (Figure 12) never reached the ultra enhanced level (say, $sSFR_{enh} > 1$, corresponding to more than 10 times sSFR enhancement compared with the median of the matching controls) as their pseudobulge counterparts. However, as the outstanding cases in classical SFGs, three of them have very low B/T. The other one J17045088+3448529 with $B/T = 0.48$, as well the "blue" bulge dominated galaxy J13151726+4424255 whose $sSFR_{enh}$ reaches almost to 0.7 as we talked about Figure 5 (also see the most upper-right data point in Figure 8), are located in low density environment (N_{1Mpc} equal to 4 and 3, respectively).

Though KPAIR (Domingue et al. 2009) was selected from allsky, strict selection criteria make it a relatively small sample. After further refining the classifications such as separating the sample into S+S/S+E pair or pseudo/classical bulge, the subsamples sometimes are too small for a very robust for a robust statistical analysis. Nevertheless, the individual case studies in this paper provide a perspective of the complex mechanism of the interaction-induced star formation enhancement. Future sky surveys with deeper sensitivities and sharper resolutions (e.g., Euclid) will produce larger and better samples for more conclusive studies.

6. Conclusion

Here we present a study of SFGs with pseudobulges (bulges with Sérsic index $n < 2$) in a local close major-merger galaxy pair sample (H-KPAIR). The sample is taken from He et al. (2022) who did 2-D GALFIT decompositions to study the B/T dependence of the star formation enhancement of paired SFGs. New aperture photometries in the SDSS *u*, *r*, *i*-bands and the

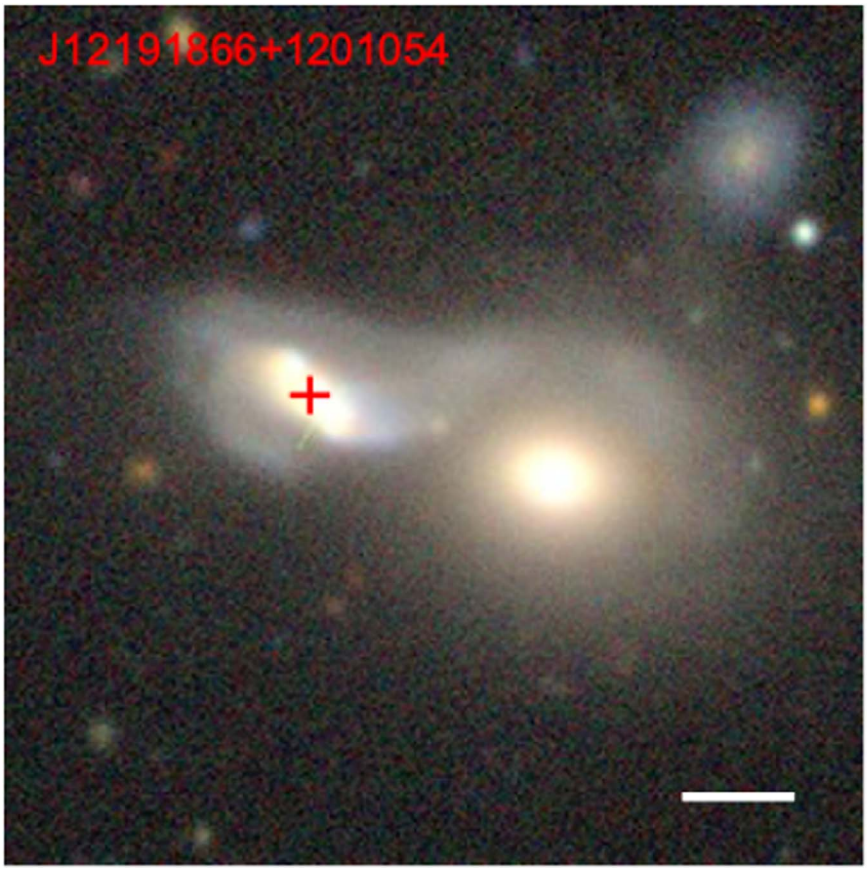

Figure 15. DESI images of J1219+1200, an S+E pair. S component, J12191866+1201054 (identified by a red plus sign), is a pseudobulge SFG that contains a bar. The white dash on the bottom-right corner of the figure illustrates the angular scale of 10″.

2MASS K_s-band are carried out for the sample to investigate the stellar populations in the central part (D = 7 kpc) of the galaxies. With the new data and data from the literature, we obtain the following results:

1. The mean Age of central stellar populations in spiral galaxies with classical bulges increases with the B/T ratio. On the other hand, the mean Age of central stellar populations in Spirals with pseudobulges is nearly constant against the B/T ratio and is consistent with the mean Age of central stellar populations of disky galaxies (with B/T $\sim$ 0). This confirms that the pseudobulges in the sample are associated mainly with disky phenomena such as bars, nuclear rings, and bright nuclei.
2. Spiral galaxies have a modestly reduced fraction of pure disk galaxies than in single Spirals, which can be due to the misidentifying as a large pseudobulge of the nuclear/circum-nuclear starburst phenomena.
3. Compared with SFGs with classical bulges, those with pseudobulges have a 2σ higher mean of sSFR enhancement ($\mathrm{sSFR_{enh}} = 0.33 \pm 0.07$ vs $\mathrm{sSFR_{enh}} = 0.12 \pm 0.06$) and much broader scatter ($\sim$1 dex).
4. The eight SFGs that have the highest $\mathrm{sSFR_{enh}}$ in the sample are all pseudobulge galaxies. A majority (69%) of paired SFGs with strong enhancement (having sSFR more than 5 times the median of the control galaxies) have pseudobulges. The Spitzer data show that the pseudobulges in these galaxies are tightly linked to nuclear starbursts. These results suggest that nuclear starburst may be the dominant mode for strong tidally induced star formation in paired galaxies.
5. Pseudobulge SFGs in S+S and in S+E pairs have 3σ significantly different sSFR enhancement: the mean $\mathrm{sSFR_{enh}} = 0.45 \pm 0.08$ and -0.04 ± 0.11 for the former and latter, respectively. A high fraction (5/11) of pseudobulge SFGs in S+E are in rich groups/clusters (local density $N_{1\mathrm{Mpc}} \geqslant 7$), whose star formation enhancement may be hindered by the environment.

In conclusion, we find that paired SFGs with pseudobulges have very diversified central stellar populations and sSFR enhancements. They include galaxies with bars, inner disks and rings, and strong nuclear/circum-nuclear starbursts. The SFGs with strong sSFR enhancement are dominated by pseudobulge

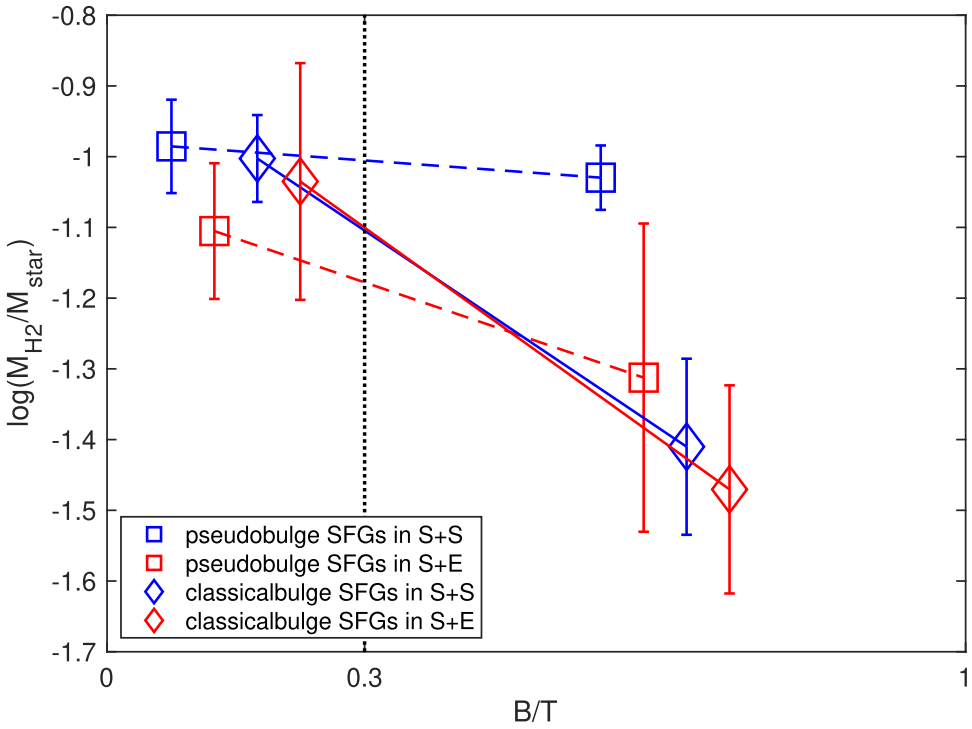

Figure 16. Plot of means of $\log(M_{H2}/M\text{star})$ and errors in two B/T bins for pseudobulge SFGs (square) and classical bulge SFGs (diamond) in S+S (blue) and S+E (red) pair.

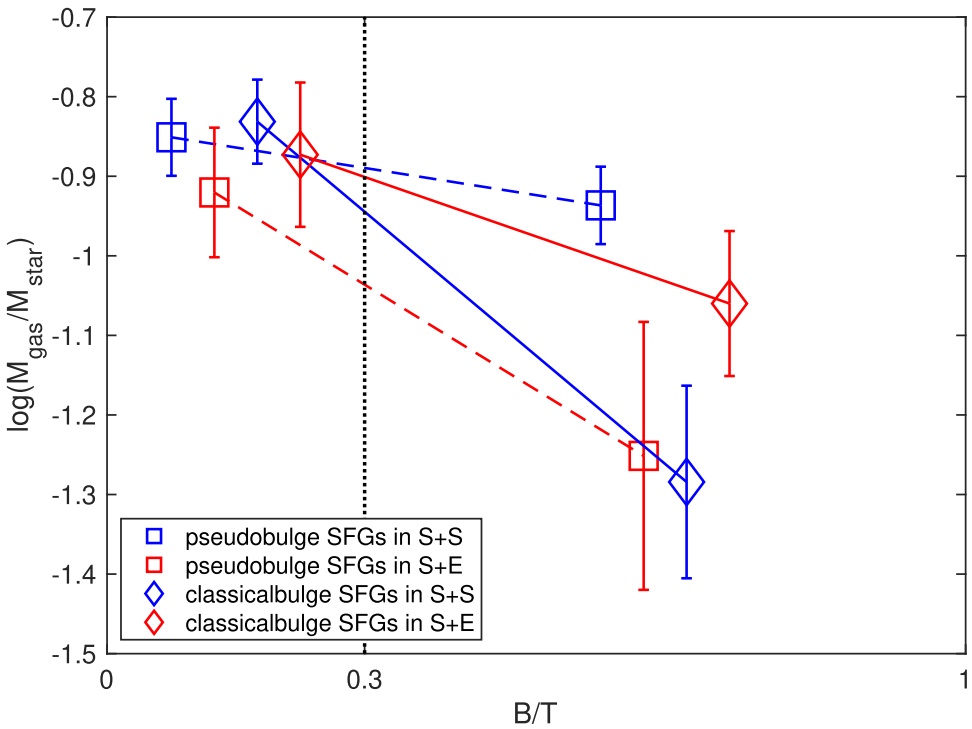

Figure 17. Plot of means of $\log(M_{\text{gas}}/M\text{star})$ and errors in two B/T bins for pseudobulge SFGs (squares) and classical bulge SFGs (diamonds) in S+S (blue) and S+E (red) pair.

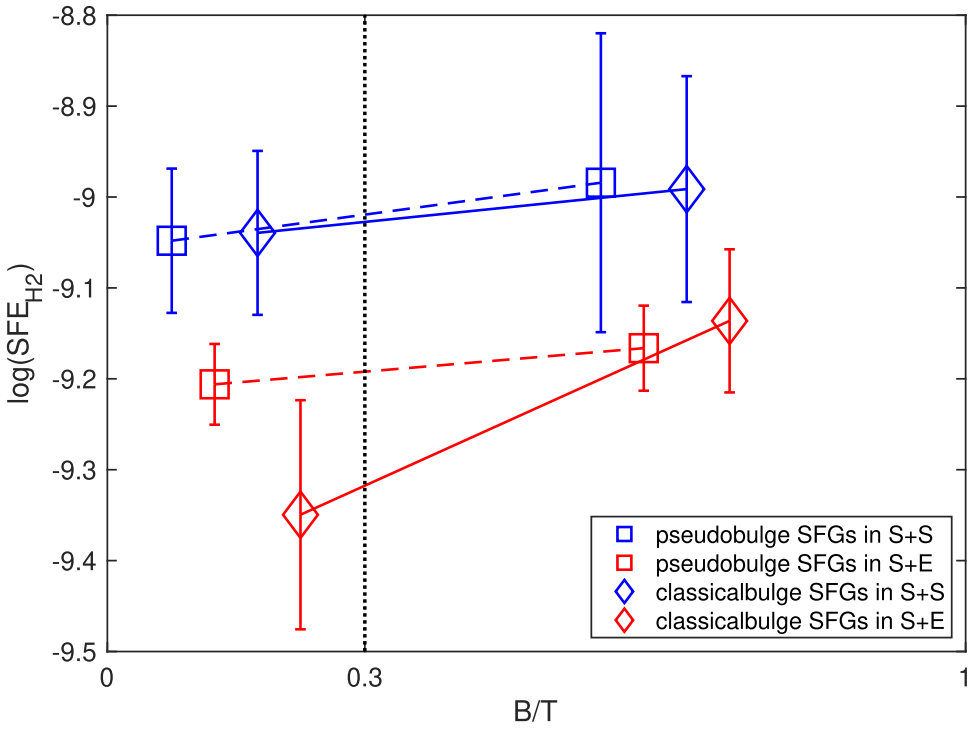

Figure 18. Plot of means of log(SFE$_{H2}$) and errors in two B/T bins for pseudobulge SFGs (squares) and classical bulge SFGs (diamonds) in S+S (blue) and S+E (red) pair.

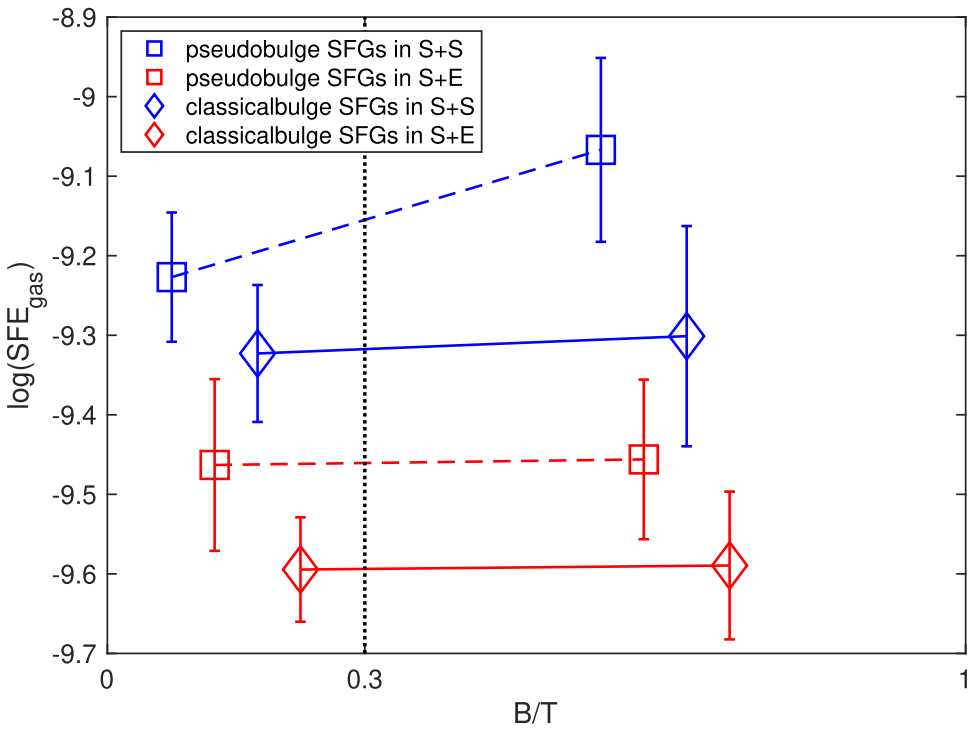

Figure 19. Plot of means of log(SFE$_{gas}$) and errors in two B/T bins for pseudobulge SFGs (squares) and classical bulge SFGs (diamonds) in S+S (blue) and S+E (red) pair.

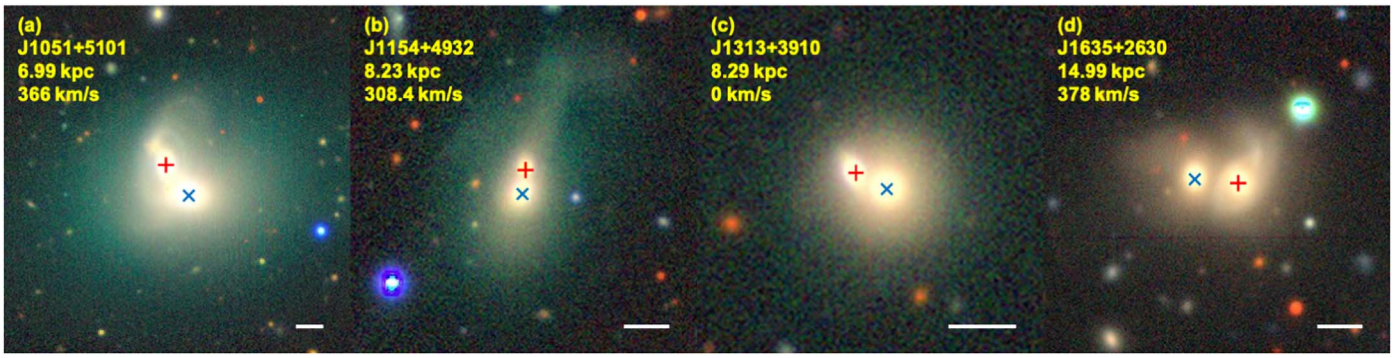

Figure 20. DESI images of four late-stage S+E mergers. The red plus signs mark the S components and the blue crosses the E components. The white dash on the bottom-right corner of each stamp illustrates the angular scale of 10″. The pair projected separation and radial velocity difference are provided as well.

Table 4
Galaxies in Late-stage S+E Mergers

Name	z	Type	$\log M_{\rm star}$ ($M_\odot$)	sSFR	$\log M_{\rm gas}$ ($M_\odot$)	SDSS_id	GROUP_id	Richness	Rank
(1)	(2)	(3)	(4)	(5)	(6)	(7)	(8)	(9)	(10)
J10514368+5101195	0.0250	E	11.12	−11.86	8.71	189845	1745	12	1
J10514450+5101303	0.0238	S	10.85	−11.64	<8.66	189846	1745	12	2
J11542299+4932509	0.0702	S	10.98	−11.35	9.49	…	…	…	…
J11542307+4932456	0.0712	E	11.35	−11.72	<9.48	229360	215518	1	1
J13131429+3910360	0.0716	E	11.26	−11.43	<9.36	445348	47	103	1
J13131470+3910382	0.0716	S	10.95	−11.12	<9.48	445349	47	103	2
J16354293+2630494	0.0701	S	11.27	−11.31	<9.52	…	…	…	…
J16354366+2630505	0.0713	E	11.27	−11.63	<9.55	306304	177	49	1

Note. The columns are: (1) galaxy name; (2) redshift; (3) galaxy morphology: "S" for Spiral, "E" for Elliptical; (4) stellar mass; (5) specific star formation rate; (6) total gas mass from dust mass (Cao et al. 2016); (7) SDSS-ID; (8) Group-ID; (9) richness (i.e., number of galaxies in the group); (10) rank (1 = most massive, 2 = other galaxies). Data in column (7)–(10) are from Yang et al. (2012). Those galaxies with no data in columns (7)–(10) are not included in the catalog of Yang et al. (2012) for lack of spectroscopic redshift.

galaxies with nuclear/circum-nuclear starbursts. On the other hand, many pseudobulge SFGs, particularly those in S+E pairs, are barred or ringed galaxies with old central stellar populations and low sSFR enhancements, which are probably caused by environmental effects.

Acknowledgments

This work is supported by the National Natural Science Foundation of China (NSFC) No. 11873055 and No.11933003, and is sponsored (in part) by the Chinese Academy of Sciences (CAS) through a grant to the CAS South America Center for Astronomy (CASSACA). U.L. acknowledges support from project PID2020-114414GB-100, financed by MCIN/AEI/10.13039/501100011033 and from the Junta de Andaluciaía (Spain) grant FQM108. T.F. and Q.Y. acknowledge support by the National Key R&D Program of China No. 2017YFA0402600, the National Natural Science Foundation of China (NSFC) grant Nos. 11890692, 12133008, and 12221003 and China Manned Space Project No. CMS-CSST-2021-A04.

The authors would like to thank Gaoxiang Jin, Cheng Cheng, Chen Cao, Yilun Wang, and Yufu Shen for their helpful discussions.

This publication makes use of data products from the Sloan Digital Sky Survey (SDSS). Funding for the Sloan Digital Sky Survey IV has been provided by the Alfred P. Sloan Foundation, the U.S. Department of Energy Office of Science, and the Participating Institutions. SDSS acknowledges support and resources from the Center for High-Performance Computing at the University of Utah. The SDSS website is

www.sdss.org. SDSS is managed by the Astrophysical Research Consortium for the Participating Institutions of the SDSS Collaboration including the Brazilian Participation Group, the Carnegie Institution for Science, Carnegie Mellon University, Center for Astrophysics | Harvard & Smithsonian (CfA), the Chilean Participation Group, the French Participation Group, Instituto de Astrofísica de Canarias, The Johns Hopkins University, Kavli Institute for the Physics and Mathematics of the Universe (IPMU) / University of Tokyo, the Korean Participation Group, Lawrence Berkeley National Laboratory, Leibniz Institut für Astrophysik Potsdam (AIP), Max-Planck-Institut für Astronomie (MPIA Heidelberg), Max-Planck-Institut für Astrophysik (MPA Garching), Max-Planck-Institut für Extraterrestrische Physik (MPE), National Astronomical Observatories of China, New Mexico State University, New York University, University of Notre Dame, Observatório Nacional / MCTI, The Ohio State University, Pennsylvania State University, Shanghai Astronomical Observatory, United Kingdom Participation Group, Universidad Nacional Autónoma de México, University of Arizona, University of Colorado Boulder, University of Oxford, University of Portsmouth, University of Utah, University of Virginia, University of Washington, University of Wisconsin, Vanderbilt University, and Yale University.

This publication makes use of data products from the Two Micron All Sky Survey, which is a joint project of the University of Massachusetts and the Infrared Processing and Analysis Center/California Institute of Technology, funded by the National Aeronautics and Space Administration and the National Science Foundation.

This publication makes use of image products from the Dark Energy Spectroscopic Instrument (DESI). DESI construction and operations is managed by the Lawrence Berkeley National Laboratory. This research is supported by the U.S. Department of Energy, Office of Science, Office of High-Energy Physics, under Contract No. DE–AC02–05CH11231, and by the National Energy Research Scientific Computing Center, a DOE Office of Science User Facility under the same contract. Additional support for DESI is provided by the U.S. National Science Foundation, Division of Astronomical Sciences under Contract No. AST-0950945 to the NSF's National Optical-Infrared Astronomy Research Laboratory; the Science and Technologies Facilities Council of the United Kingdom; the Gordon and Betty Moore Foundation; the Heising-Simons Foundation; the French Alternative Energies and Atomic Energy Commission (CEA); the National Council of Science and Technology of Mexico (CONACYT); the Ministry of Science and Innovation of Spain, and by the DESI Member Institutions. The DESI collaboration is honored to be permitted to conduct astronomical research on Iolkam Du'ag (Kitt Peak), a mountain with particular significance to the Tohono O'odham Nation.

ORCID iDs

Chuan He (何川) https://orcid.org/0000-0003-1761-5442
Cong Xu (徐聪) https://orcid.org/0000-0002-1588-6700
Ute Lisenfeld https://orcid.org/0000-0002-9471-5423
Yu Sophia Dai (戴昱) https://orcid.org/0000-0002-7928-416X
Taotao Fang (方陶陶) https://orcid.org/0000-0002-2853-3808
Jiasheng Huang (黄家声) https://orcid.org/0000-0001-6511-8745
Wei Wang (王炜) https://orcid.org/0000-0002-9702-4441
Qingzheng Yu (余清正) https://orcid.org/0000-0003-3230-3981

References

Alonso, M. S., Tissera, P. B., Coldwell, G., & Lambas, D. G. 2004, MNRAS, 352, 1081
Barnes, J. E., & Hernquist, L. 1996, ApJ, 471, 115
Bertin, E., Mellier, Y., Radovich, M., et al. 2002, in ASP Conf. Ser. 281, Astronomical Data Analysis Software and Systems XI, ed. D. A. Bohlender, D. Durand, & T. H. Handley (San Francisco, CA: ASP), 228
Bluck, A. F. L., Mendel, J. T., Ellison, S. L., et al. 2014, MNRAS, 441, 599
Bruzual, G., & Charlot, S. 2003, MNRAS, 344, 1000
Cao, C., Xu, C. K., Domingue, D., et al. 2016, ApJS, 222, 16
Cardelli, J. A., Clayton, G. C., & Mathis, J. S. 1989, ApJ, 345, 245
Chown, R., Li, C., Athanassoula, E., et al. 2019, MNRAS, 484, 5192
Cox, T. J., Jonsson, P., Somerville, R. S., Primack, J. R., & Dekel, A. 2008, MNRAS, 384, 386
Di Matteo, P., Bournaud, F., Martig, M., et al. 2008, A&A, 492, 31
Di Matteo, P., Combes, F., Melchior, A. L., & Semelin, B. 2007, A&A, 468, 61
Domingue, D. L., Xu, C. K., Jarrett, T. H., & Cheng, Y. 2009, ApJ, 695, 1559
Driver, S. P., Allen, P. D., Graham, A. W., et al. 2006, MNRAS, 368, 414
Ellison, S. L., Patton, D. R., Simard, L., et al. 2010, MNRAS, 407, 1514
Erwin, P., Seth, A., Debattista, V. P., et al. 2021, MNRAS, 502, 2446
Feng, S., Shen, S.-Y., Yuan, F.-T., Riffel, R. A., & Pan, K. 2020, ApJL, 892, L20
Fraser-McKelvie, A., Merrifield, M., Aragón-Salamanca, A., et al. 2020, MNRAS, 499, 1116
Gavazzi, G., Boselli, A., Cortese, L., et al. 2006, A&A, 446, 839
Giovanelli, R., & Haynes, M. P. 1983, AJ, 88, 881
Gunn, J. E., Gott, J., & Richard, I. 1972, ApJ, 176, 1
He, C., Xu, C. K., Domingue, D., Cao, C., & Huang, J.-s. 2022, ApJS, 261, 34
Herrera-Endoqui, M., Salo, H., Laurikainen, E., & Knapen, J. H. 2017, A&A, 599, A43
Holincheck, A. J., Wallin, J. F., Borne, K., et al. 2016, MNRAS, 459, 720
Hopkins, P. F., Cox, T. J., Younger, J. D., & Hernquist, L. 2009, ApJ, 691, 1168
Hwang, H. S., Elbaz, D., Dickinson, M., et al. 2011, A&A, 535, A60
Hwang, H. S., Elbaz, D., Lee, J. C., et al. 2010, A&A, 522, A33
Keel, W. C., Kennicutt, R. C. J., Hummel, E., & van der Hulst, J. M. 1985, AJ, 90, 708
Kennicutt, R. C. J. 1998, ARA&A, 36, 189
Kennicutt, R. C. J., Keel, W. C., van der Hulst, J. M., Hummel, E., & Roettiger, K. A. 1987, AJ, 93, 1011
Kim, K., Oh, S., Jeong, H., et al. 2016, ApJS, 225, 6
Kormendy, J., & Ho, L. C. 2013, ARA&A, 51, 511
Kormendy, J., & Kennicutt, R. C. J. 2004, ARA&A, 42, 603
Larson, R. B., & Tinsley, B. M. 1978, ApJ, 219, 46
Li, Y. A., Ho, L. C., & Shangguan, J. 2023, ApJ, 953, 91
Lintott, C. J., Schawinski, K., Slosar, A., et al. 2008, MNRAS, 389, 1179
Lisenfeld, U., Xu, C. K., Gao, Y., et al. 2019, A&A, 627, A107
Madau, P., & Dickinson, M. 2014, ARA&A, 52, 415
Martig, M., Bournaud, F., Teyssier, R., & Dekel, A. 2009, ApJ, 707, 250
Meert, A., Vikram, V., & Bernardi, M. 2015, MNRAS, 446, 3943
Mihos, J. C., & Hernquist, L. 1996, ApJ, 464, 641
Moon, J.-S., An, S.-H., & Yoon, S.-J. 2019, ApJ, 882, 14

Moon, J.-S., An, S.-H., & Yoon, S.-J. 2021, ApJ, 909, 34
Moore, B., Lake, G., & Katz, N. 1998, ApJ, 495, 139
Nikolic, B., Cullen, H., & Alexander, P. 2004, MNRAS, 355, 874
Pan, H.-A., Lin, L., Hsieh, B.-C., et al. 2019, ApJ, 881, 119
Park, C., & Choi, Y.-Y. 2009, ApJ, 691, 1828
Patton, D. R., Torrey, P., Ellison, S. L., Mendel, J. T., & Scudder, J. M. 2013, MNRAS, 433, L59
Peng, Y.-j., Lilly, S. J., Kovač, K., et al. 2010, ApJ, 721, 193
Peng, Y.-j., Lilly, S. J., Renzini, A., & Carollo, M. 2012, ApJ, 757, 4
Rodighiero, G., Daddi, E., Baronchelli, I., et al. 2011, ApJL, 739, L40
Sanders, D. B., & Mirabel, I. F. 1996, ARA&A, 34, 749
Sargent, A., & Scoville, N. 1991, ApJL, 366, L1
Scoville, N. Z., Sargent, A. I., Sanders, D. B., & Soifer, B. T. 1991, ApJL, 366, L5
Scudder, J. M., Ellison, S. L., Torrey, P., Patton, D. R., & Mendel, J. T. 2012, MNRAS, 426, 549
Steffen, J. L., Fu, H., Comerford, J. M., et al. 2021, ApJ, 909, 120
Toomre, A., & Toomre, J. 1972, ApJ, 178, 623
Xu, C., & Sulentic, J. W. 1991, ApJ, 374, 407
Xu, C. K., Domingue, D., Cheng, Y.-W., et al. 2010, ApJ, 713, 330
Xu, C. K., Lisenfeld, U., Gao, Y., & Renaud, F. 2021, ApJ, 918, 55
Yang, X., Mo, H. J., van den Bosch, F. C., Zhang, Y., & Han, J. 2012, ApJ, 752, 41
Zuo, P., Xu, C. K., Yun, M. S., et al. 2018, ApJS, 237, 2